Defense Threat Reduction Agency
8725 John J. Kingman Road, MS
6201 Fort Belvoir, VA 22060-6201

TECHNICAL REPORT

Development of Compositionally Graded Metallic Glass Alloys with Desirable Properties

June 2016

Dr. Wolfgang Windl

Prepared by:
The Ohio State University
1960 Kenny Rd.
Columbus, OH 43210

REPORT DOCUMENTATION PAGE

The public reporting burden for this collection of information is estimated to average 1 hour per response, including the time for reviewing instructions, searching existing data sources, gathering and maintaining the data needed, and completing and reviewing the collection of information. Send comments regarding this burden estimate or any other aspect of this collection of information, including suggestions for reducing the burden, to Department of Defense, Washington Headquarters Services, Directorate for Information Operations and Reports (0704-0188), 1215 Jefferson Davis Highway, Suite 1204, Arlington, VA 22202-4302. Respondents should be aware that notwithstanding any other provision of law, no person shall be subject to any penalty for failing to comply with a collection of information if it does not display a currently valid OMB control number. **PLEASE DO NOT RETURN YOUR FORM TO THE ABOVE ADDRESS.**

1. REPORT DATE (DD-MM-YYYY) 00-06-2016	2. REPORT TYPE Final Technical Report	3. DATES COVERED (From - To) 11-Jul-2011 - 17-Jul-2015

4. TITLE AND SUBTITLE
Development of compositionally graded metallic glass alloys with desirable properties

5a. CONTRACT NUMBER

5b. GRANT NUMBER
HDTRA1-11-1-0047

5c. PROGRAM ELEMENT NUMBER

6. AUTHOR(S)
Wolfgang Windl

5d. PROJECT NUMBER

5e. TASK NUMBER

5f. WORK UNIT NUMBER

7. PERFORMING ORGANIZATION NAME(S) AND ADDRESS(ES)
The Ohio State University
1960 Kenny Rd Columbus OH 43210-1016

8. PERFORMING ORGANIZATION REPORT NUMBER

9. SPONSORING/MONITORING AGENCY NAME(S) AND ADDRESS(ES)
Defense Threat Reduction Agency
8725 John J. Kingman Road
Fort Belvoir, VA 22060-6201

10. SPONSOR/MONITOR'S ACRONYM(S)
DTRA

11. SPONSOR/MONITOR'S REPORT NUMBER(S) DTRA-TR-16-69

12. DISTRIBUTION/AVAILABILITY STATEMENT
Distribution Statement A. Approved for public release; distribution is unlimited.

13. SUPPLEMENTARY NOTES

14. ABSTRACT
In this work the grantees use a combination of experimental and computational tools to design and produce compositionally graded metallic glass alloys with desirable properties, particularly for the extreme conditions of ballistic impact.

15. SUBJECT TERMS
metallic glass alloys; ballistic, high kinetic energy; penetrating properties

16. SECURITY CLASSIFICATION OF:			17. LIMITATION OF ABSTRACT	18. NUMBER OF PAGES	19a. NAME OF RESPONSIBLE PERSON
a. REPORT	b. ABSTRACT	c. THIS PAGE	SAR	59	Allen Dalton
U	U	U			19b. TELEPHONE NUMBER (Include area code) 703-767-3054

UNIT CONVERSION TABLE
U.S. customary units to and from international units of measurement[*]

U.S. Customary Units	Multiply by → ← Divide by[†]		International Units
Length/Area/Volume			
inch (in)	2.54	$\times 10^{-2}$	meter (m)
foot (ft)	3.048	$\times 10^{-1}$	meter (m)
yard (yd)	9.144	$\times 10^{-1}$	meter (m)
mile (mi, international)	1.609 344	$\times 10^{3}$	meter (m)
mile (nmi, nautical, U.S.)	1.852	$\times 10^{3}$	meter (m)
barn (b)	1	$\times 10^{-28}$	square meter (m^2)
gallon (gal, U.S. liquid)	3.785 412	$\times 10^{-3}$	cubic meter (m^3)
cubic foot (ft^3)	2.831 685	$\times 10^{-2}$	cubic meter (m^3)
Mass/Density			
pound (lb)	4.535 924	$\times 10^{-1}$	kilogram (kg)
unified atomic mass unit (amu)	1.660 539	$\times 10^{-27}$	kilogram (kg)
pound-mass per cubic foot (lb ft^{-3})	1.601 846	$\times 10^{1}$	kilogram per cubic meter (kg m^{-3})
pound-force (lbf avoirdupois)	4.448 222		newton (N)
Energy/Work/Power			
electron volt (eV)	1.602 177	$\times 10^{-19}$	joule (J)
erg	1	$\times 10^{-7}$	joule (J)
kiloton (kt) (TNT equivalent)	4.184	$\times 10^{12}$	joule (J)
British thermal unit (Btu) (thermochemical)	1.054 350	$\times 10^{3}$	joule (J)
foot-pound-force (ft lbf)	1.355 818		joule (J)
calorie (cal) (thermochemical)	4.184		joule (J)
Pressure			
atmosphere (atm)	1.013 250	$\times 10^{5}$	pascal (Pa)
pound force per square inch (psi)	6.984 757	$\times 10^{3}$	pascal (Pa)
Temperature			
degree Fahrenheit (°F)	[T(°F) − 32]/1.8		degree Celsius (°C)
degree Fahrenheit (°F)	[T(°F) + 459.67]/1.8		kelvin (K)
Radiation			
curie (Ci) [activity of radionuclides]	3.7	$\times 10^{10}$	per second (s^{-1}) [becquerel (Bq)]
roentgen (R) [air exposure]	2.579 760	$\times 10^{-4}$	coulomb per kilogram (C kg^{-1})
rad [absorbed dose]	1	$\times 10^{-2}$	joule per kilogram (J kg^{-1}) [gray (Gy)]
rem [equivalent and effective dose]	1	$\times 10^{-2}$	joule per kilogram (J kg^{-1}) [sievert (Sv)]

[*]Specific details regarding the implementation of SI units may be viewed at http://www.bipm.org/en/si/.
[†]Multiply the U.S. customary unit by the factor to get the international unit. Divide the international unit by the factor to get the U.S. customary unit.

2015-11-16

Grant/Award #: HDTRA1-11-1-0047
PI Name: Dr. Wolfgang Windl, Professor
Organization/Institution: The Ohio State University
Co-PI; Dr. Katharine Flores, Professor (Washington University St Louis)
Project Title: Development of compositionally graded metallic glass alloys with desirable properties

What are the major goals of the project?
List the major goals of the project as stated in the approved application or as approved by the agency. If the application lists milestones/target dates for important activities or phases of the project, identify these dates and show actual completion dates or the percentage of completion. Generally, the goals will not change from one reporting period to the next. However, if the awarding agency approved changes to the goals during the reporting period, list the revised goals and objectives. Also explain any significant changes in approach or methods from the agency approved application or plan.

In this work the grantees use a combination of experimental and computational tools to design and produce *compositionally graded* metallic glass alloys with desirable properties, particularly for the extreme conditions of ballistic impact. This research is in direct response to Topic Per5-G: "Amorphous Metals for High-Performance Penetration" of the solicitation this project responded to. This topic is defined within DTRA Basic Research Thrust Area 4: "Science to Defeat WMD." The fabrication of metallic glasses with graded composition pursued in the current project will enable the manufacture of structures with graded properties for improved penetration and payload delivery, such as an outer shell that is hard and remains smooth on the outer surface but tough in the interior.

The scope of the overall project encompasses three technical objectives:

- Proof of concept – demonstrate that graded metallic glass coatings influence the transmission of high-kinetic energy penetrators through sand layers positively
- Show that graded metallic glass layers can indeed be fabricated, along with identification of their composition-dependent glass forming ability and mechanical properties
- Explore possible compositions and composition gradients through computations

On the technical side, these three major milestones are achieved by the following innovations:

- Develop a finite-element model that allows to explore penetrating properties of projectiles with different surface layers, especially those with graded properties.
- Use computational modeling to establish novel, physics-based predictive rules for glass forming ability in systems of 2 or 3 elements. Produce small batches of candidate alloy compositions for rapid model validation, using a laser deposition technique to permit rapid and efficient evaluation of the alloy structure and glass stability.
- Using the simple 2 or 3 element alloys identified by the computation-based optimization process as a starting point, produce compositionally graded alloys of multicomponent (≥3 component) systems via laser deposition. Use this combinatorial technique to refine the alloy compositions for optimal glass forming ability and other properties. Produce the most promising compositions in bulk via casting techniques for further characterization.

Year 5 of the project should have concentrated on designing, fabricating, and testing alloys with desirable properties, such as high strength under dynamic loading, based on the previous work.

1. PROOF OF CONCEPT THROUGH CONTINUUM SIMULATIONS

1.1 Summary

Finite element (FE) simulations were performed to assess the hypothesis that metallic glass projectiles with graded properties would perform better as penetrators than homogenous projectiles. In the simulation a metallic glass projectile impacts and travels through dry sand. The kinetic energy and damage to the projectile are tracked as a function of depth. A second set of simulations were performed where after traveling through the sand to a specified depth the projectile impacts and penetrates a reinforced concrete slab. Two different grading schemes were considered i) grading of properties from front to rear of the projectile and ii) and radial grading from properties from inner core to outer skin. Projectiles with homogenous properties were also explored. As expected in the homogenous case the penetration depth was positively correlated with increasing density, elastic stiffness, and compressive strength. For the graded projectiles grading density along the length (from highest density at the nose to lowest density at the rear) was found to produce ~9% increase in penetration depth over the homogenous projectile. Projectiles with graded stiffness and strength along the length and projectile with radial grading of properties showed significantly smaller improvement in penetration depth.

1.2 Simulation Overview

This section serves as a brief overview of the FE simulations. A complete description of the material properties can be found in the appendix.
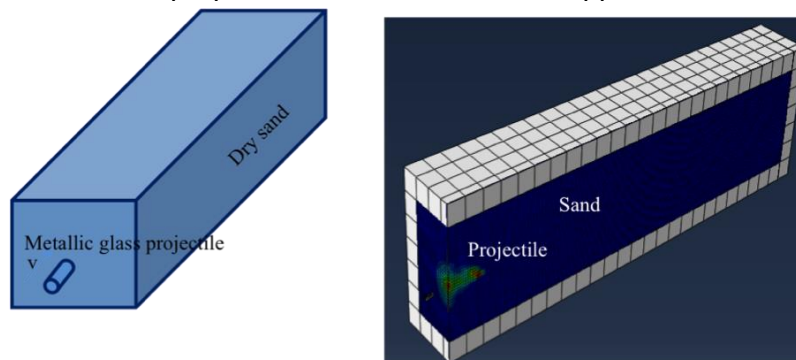

All simulations were performed using a coupled Eulerian/Lagrangian (CEL) approach in ABAQUS explicit. The sand was modeled as a Euleraian fluid and the projectile and concrete slab with an standard Lagrangian. The Eulerian part of the FE mesh in CEL analyses is represents a stationary cube which the Eulerian material (sand) can move into and out of as it interacts with the Lagrangian structures. The element may be completely or partially filled, and is tracked as it flows through the mesh as a local volume fraction in each grid. The geometry of the simulation is shown in figure 1. The Eulerian sand is constrained in a "tube" of concrete to prevent loss of sand material from the sides of the simulation volume and to mimic the constraining pressure a large body

Figure 1: Geometry of CEL FE simulation. Sand is modeled as an Eulerain fluid while the concrete and projectile as Lagrangian solids.

3

of sand (semi-infinite) would apply in a small simulation volume. The projectile is given an initial velocity of 600 m/s in air before impacting the sand.

$Zr_{55}Al_{30}Ni_5Cu_{30}$ was chosen as the model metallic glass for the projectile as experimental values for the required dynamic material properties were available in the literature (Mashimo et al 2006). The material was assumed to be elastically isotropic with a Youngs Modulus of 86GPa and a shear modulus of 31 GPa. The yield surface was described by a Drucker-Prager model. A Mie-Gruneisen equation of state (EOS) calibrated to shock Hugoniot compression data was used to model the volumetric strains under dynamic conditions and high pressures. Hardening was handled using a Johnson-Cook plasticity model coupled with a progressive damage model. Details can be found in the appendix.

The dynamic properties of sand were taken from the DOE report "Shock Response of Dry Sand" (Brown et al 2007). An EOS model with compaction was used to model the deformation of sand under dynamic loading. An initial porosity of 40% was assumed based on Brown et al. As a bulk volume the sand behaves as an elastic solid with a shear modulus of 50 MPa. The sand begins to flow plastically at a pressure of 0.9 MPa and begin to compact. At 1.1 GPa the sand is completely compacted and all pores are crushed.

The concrete properties were taken from the numerous concrete tutorials in the ABAQUS Example Manual. These properties were calibrated to samples taken from the Koyna dam and serve as an archetype material for simulation of concrete structures under seismic loading. Damage in the concrete was modeling using the Concrete Damage Plasticity model. Note that this is a simplistic damage model and the results presented below of projectile/concrete slab interaction should not be taken quantitatively. Instead the simulation was intended to show trends in impact energies as a function of slab depth. Figure 2 shows a sequence of still images showing the impact and penetration of the concrete slab by a metallic glass projectile.
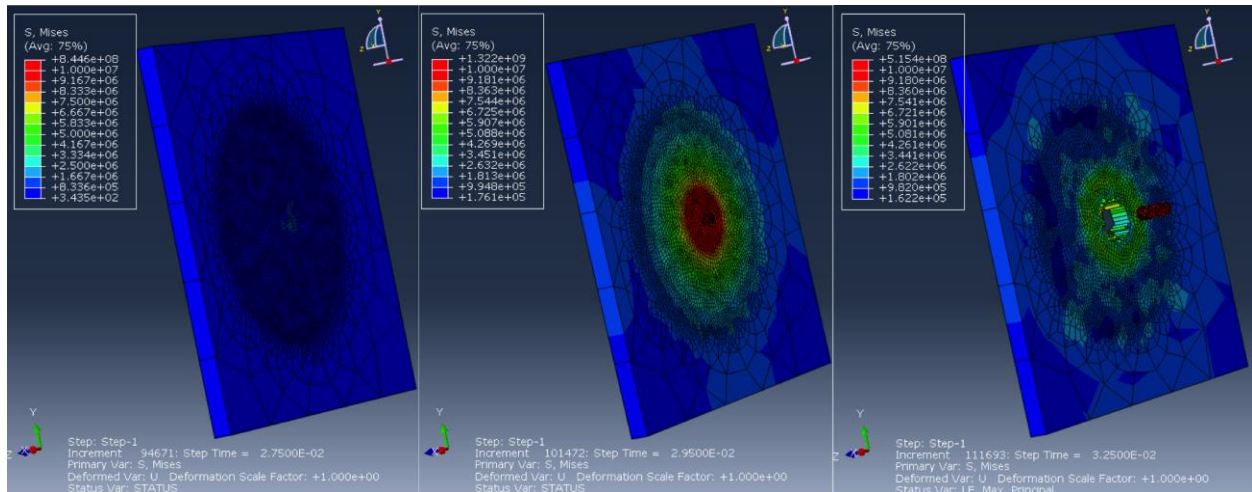

Figure 2: Impact and penetration of a concrete slab by a metallic glass projectile. The sand has been removed for clarity.

1.3 Simulation Results

1.3.1. Homogenous Metallic Glass Projectile. In order to isolate the effect of individual properties on penetration depth specific properties were perturbed from those measured for

$Zr_{55}Al_{30}Ni_5Cu_{30}$ metallic glass. Properties were perturbed independently keeping the remainder of the properties unchanged. The penetration depth of the projectile in sand was strongly correlated with increasing density, elastic stiffness, and compressive strength of the glass with density having the largest effect. Figure 3 shows the main results.

1.3.2. Graded Metallic Glass Projectile. Two different grading schemes were considered i) grading of properties from front to rear of the projectile and ii) and radial grading from properties from inner core to outer skin. The specific geometries are shown in Figure 4.

Table 1 Properties for the projectiles with along the length.

Section	Density	Stiffness	Strength
1	7200 kg/m^3 (+3%)	33.0 GPa (+5%)	1.85 GPa (+5%)
2	6790 kg/m^3	31.3 GPa	1.77 GPa
3	6500 kg/m^3 (-3%)	39.0 GPa (+5%)	1.65 GPa (-7%)

Table 1 details the properties used to explore the effect of gradients along the length. For the graded projectiles grading density along the length (from highest density at the nose to lowest density at the rear) was found to produce ~9% increase in penetration depth. Reversing the gradient direction (lowest in nose) decreased penetration depth by 5%. Grading the stiffness along the length (high to low) showed a modest improvement of 2%. When the stiffness gradient was reversed the penetration depth was virtually identical to the homogeneous projectile. Strength was an interesting case in that both positively and negatively graded structures performed better than the homogenous glass. With an 8% increase in penetration depth for the high to low graded structure and a 3% improvement for the low to high. Figure 5 and Table 2 show the key results.

For the radially graded structures no significant improvement or debit of performance was observed. Results are shown in the Appendix.
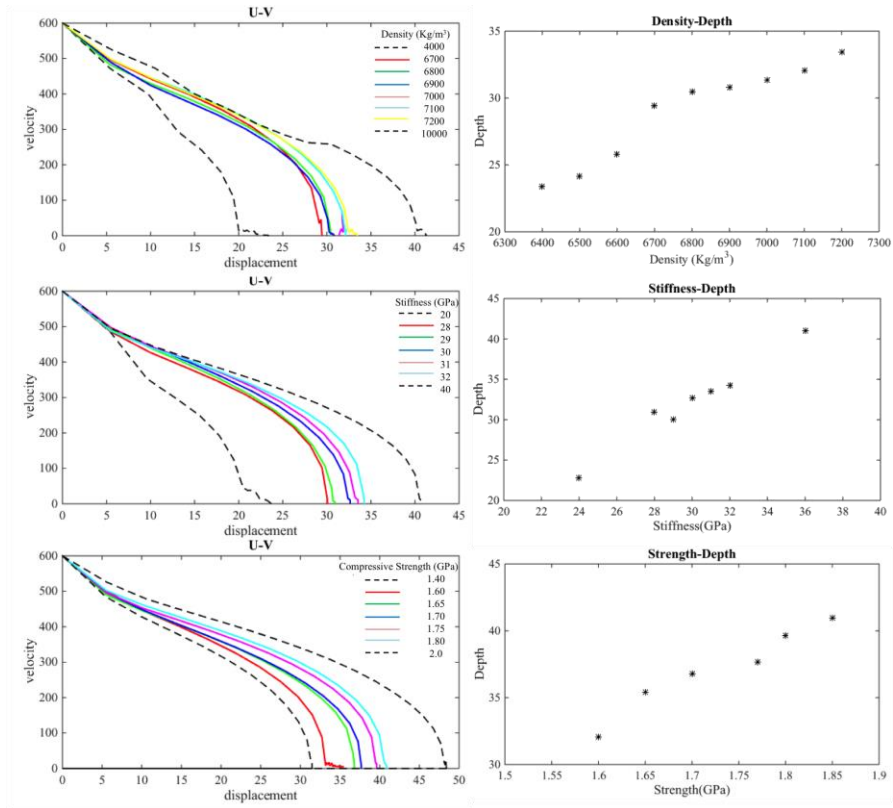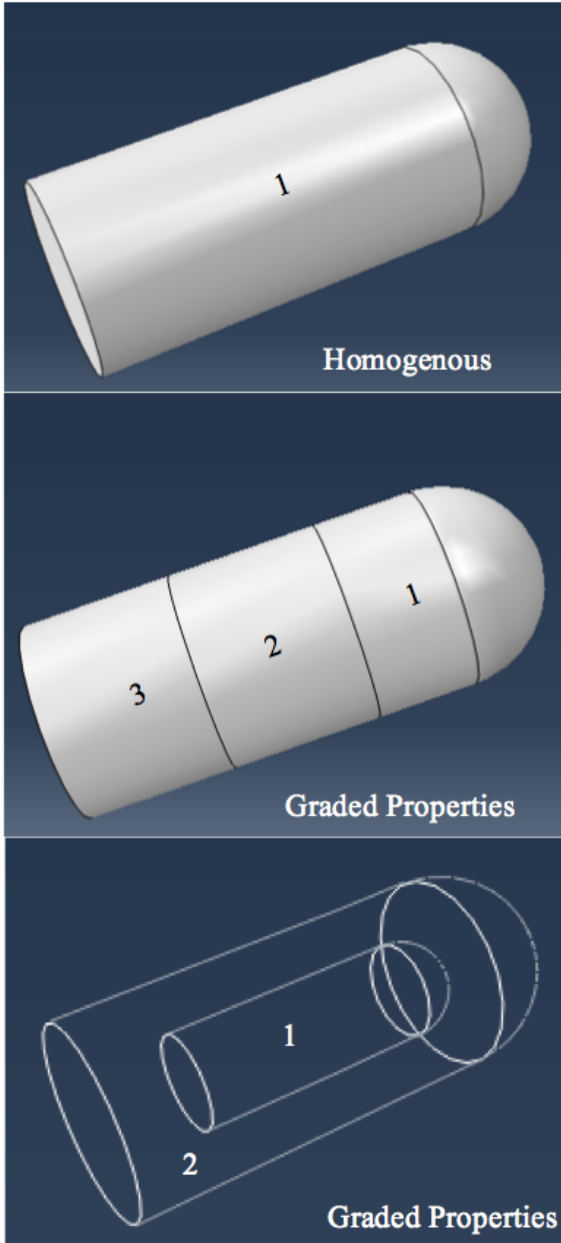
Figure 3: Trends in penetration depth for metallic glass projectiles with varying material properties.

Table 2: Penetration depth and improvement for graded metallic glass projectiles.

	Original	Density+	Density-	Stiffness+	Stiffness-	Strength+	Strength-
Penetration (m)	38.93	42.73	37.06	39.83	39.19	42.11	40.21
Improvement (%)		8.9%	(4.8%)	2.3%	0.6%	8.2%	3.3%

Material: Metallic Glass ($Zr_{55}Al_{10}Ni_5Cu_{30}$)
(Lagrangian Part)

1. Homogenous Section
    Radius: 0.2
    Length: 1
    Round: 0.2

2. Graded properties along length
    The projectile is divided in to three parts along length. Material properties are varied in each layer.

3. Graded properties along thickness
    The projectile is extruded by an inner offset part and compensate with a same size part with different properties.

Figure 4: Geometry of the graded projectiles.

Graded Properties along length(Density)

Graded Properties along length(Stiffness)

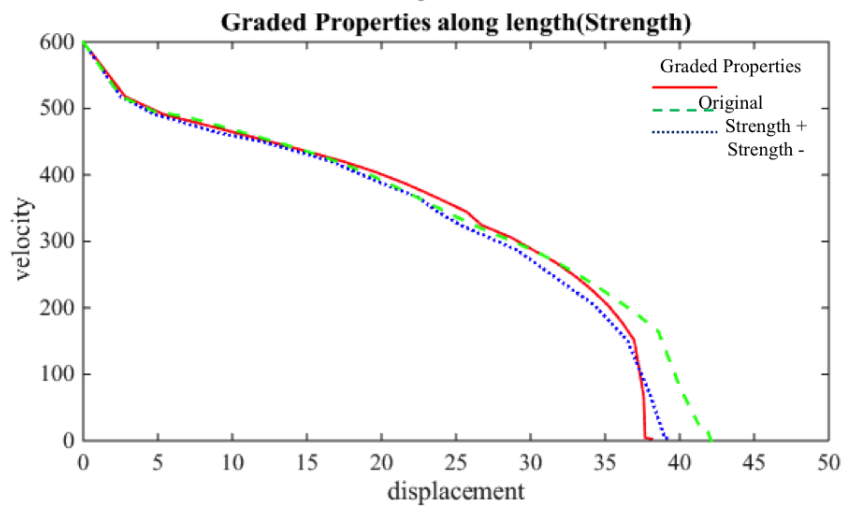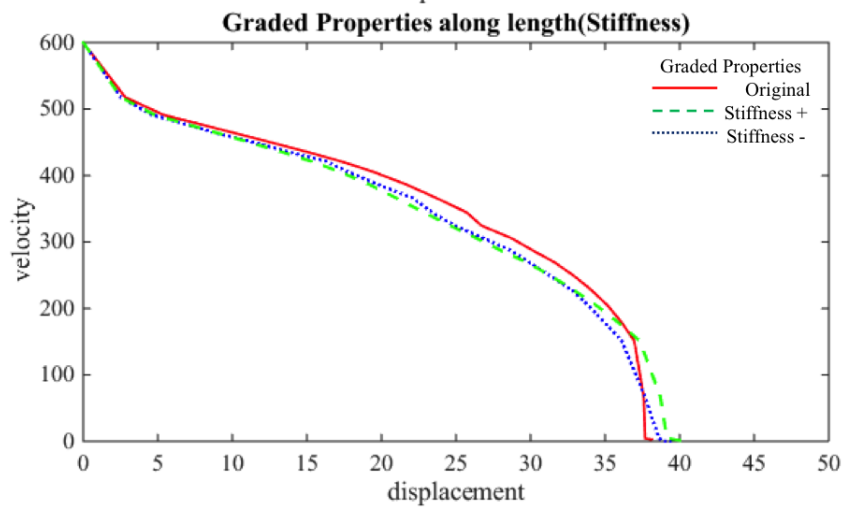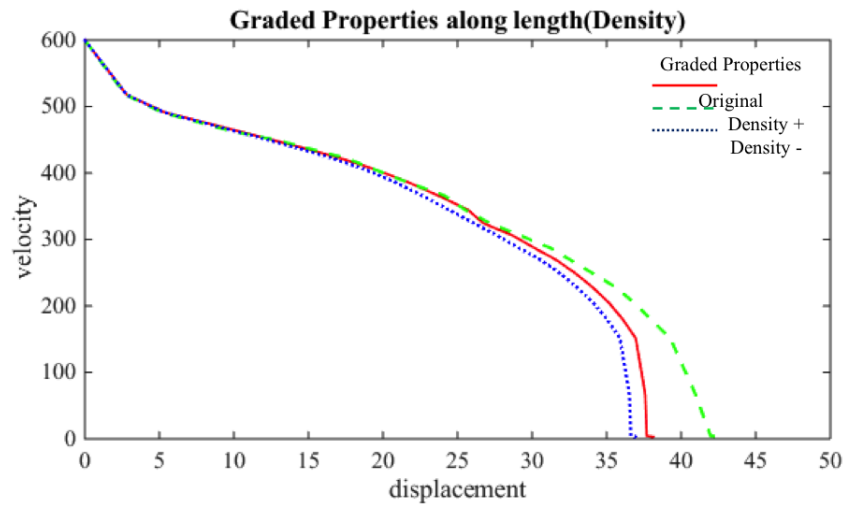## Graded Properties along length(Strength)

8

Figure 5: Velocity vs penetration depth for graded projectiles as compared to a homogenous metallic glass projectile. + indicates gradients as given by table 1 and – indicates the opposite direction (3 high and 1 low).

2. FABRICATION AND TESTING OF GRADED METALLIC GLASS LAYERS

2.1 Summary: Laser deposition as a combinatorial BMG design tool

While unresolved issues prevent the realization of fully amorphous 3-dimensional BMG parts prepared by LD,[1-4] single layer deposits nearly void of detectable crystalline features have been successfully demonstrated by co-PI Flores.[5] In addition, several groups have reported building compositionally graded crystalline specimens with LD.[6-12] Combining the two approaches, this project had as a focal goal to establish LD as a promising combinatorial tool for developing novel BMGs with desirable properties, where both composition-dependence and glass-forming ability can be studied by varying powder-feed rates and laser power in single or few-run depositions. As a proof-of-concept and method-development study, we examined the glass forming $Cu_{1-x}Zr_x$ binary system over a wide composition range and confirmed the previously reported main glass forming compositions of $Cu_{65}Zr_{35}$ and $Cu_{50}Zr_{50}$.

For the ternary Cu-Zr-Ti system, we could equally show that our fabrication scheme allows to systematically probe large regions of ternary composition space. We identified $Cu_{51.7}Zr_{36.7}Ti_{11.6}$ as the best glass former in a fraction of the experimental time of previous study, which identified similar compositions of $Cu_{57.6}Zr_{32.4}Ti_{10}$,[13] and $Cu_{60}Zr_{30}Ti_{10}$.[14]

Finally, we have demonstrated that nanoindentation along with appropriate analysis can be used on the graded LD samples to map out mechanical properties with high accuracy, thus completing a high-throughput capability to identify glass forming alloys and their mechanical properties from a large composition space.

2.2 Continuously graded Cu-Zr

As a prelude to developing novel multicomponent (3 or more elements) BMG alloys, the first experimental task was to validate the combinatorial methodology by fabricating graded binary specimens containing known BMG-forming compositions. Among binary alloys, the extensively studied Cu-Zr system was the obvious choice, due to the existence of several compositions with reported casting thicknesses of 1 mm or larger.[15,16]
All previously reported efforts to fabricate compositionally graded specimens were unsuccessful and varied the composition of the build from layer to layer by changing the relative delivery rates of two different powders. In order to overcome these problems, we have developed a two-dimensional approach to fabricate single-layer specimens that feature a compositional gradient across the surface area of the deposit.

2.2.1 Fabricating continuously graded Cu-Zr specimens by LD

All LD experiments were carried out with an Optomec MR-7 Laser Engineered Net Shaping (LENS™) system. Copper and zirconium feedstock powders with minimum purities of 99.9 and 99.2 at. %, respectively, were deposited on grade 702 Zr substrates with approximate dimensions of 3.5 cm x 4.0 cm x 0.5 cm. Prior to deposition, the substrates were surface-ground with 320 grit SiC paper and cleaned with methanol to remove any surface contaminants. To fabricate the graded Cu-Zr specimens, a square deposition geometry was chosen with dimensions

of 25.4 x 25.4 mm. Cu and Zr powders were simultaneously deposited with a 250 W laser traveling at 8.5 mm/s. To achieve compositional gradation, the delivery rate of both powders was varied in a stepwise manner from hatch to hatch along the raster path. The Cu delivery rate was gradually increased from 3.51 to 4.88 g/min while the Zr delivery rate was decreased from 3.06 to 2.36 g/min. After the initial deposit, a 200 W laser with a travel speed of 12.7 mm/s was used to create 9 re-melted lines spaced 2.54 mm apart, in the direction of the composition gradient. The re-melting step facilitated adequate localized melting and mixing of the copper and zirconium powders. The alloyed lines were then re-melted a final time with different laser powers ranging from 100 to 180 W at a higher travel speed of 16.9 mm/s.

Figure 6 shows the compositional profile of the line re-melted by a 100 W laser, measured with energy dispersive x-ray spectroscopy (EDS). The measurements were performed after polishing the entire specimen to a mirror finish with colloidal silica. The composition profile was continuously graded from 61-76 at. % Cu and is well described by a linear trend line. The predicted compositional profile based on the powder delivery rates was in excellent agreement with the measured compositional trend, confirming the ability of the experimental methodology to accurately control the compositions of graded specimens by choosing appropriate powder delivery rates.
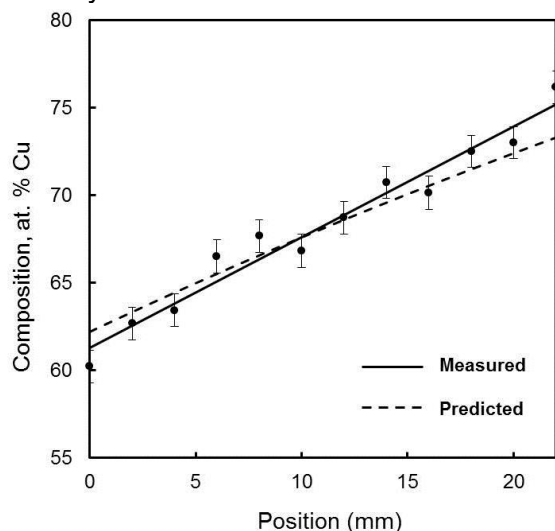

Figure 6. Compositional profile of a Cu-Zr deposit line re-melted using a laser power of 100 W and a travel speed of 16.9 mm/s. The measured profile is compared with the ideal profile predicted by the powder feed rates, assuming perfect deposition efficiency of both the Cu and Zr powders.

2.2.1 Identifying vitrified regions in the Cu-rich graded Cu-Zr specimens

In addition to the capability to rapidly synthesize compositional libraries, a complete combinatorial methodology for developing new metallic glass alloys must include a means for high-throughput screening of amorphous material within the library. X-ray and electron diffraction are the most dependable techniques for verifying amorphous structure. However, conventional x-ray diffraction techniques are limited to interrogating relatively large (millimeter-scale) areas, while micro-XRD and electron diffraction often requires several hours to prepare and analyze a single composition. Therefore, they are not ideal for the rapid screening of metallic glass-forming regions in large compositional libraries.

As an alternative, Ding et al.[21] reported a high-throughput approach by distinguishing amorphous from crystalline material by inspection of surface topography. They showed that for unconstrained solidification as we have here, a smooth, featureless topography is indicative of glass formation, whereas crystalline features form visibly distinct asperities.

Preliminary identification of potential glass-forming compositions in the compositionally-graded Cu-Zr specimens was accomplished using a Nikon light microscope equipped with differential interference contrast (DIC) for enhanced imaging of the specimen's three-dimensional surface topography. In addition, DIC microscopy is capable of detecting surface asperities with
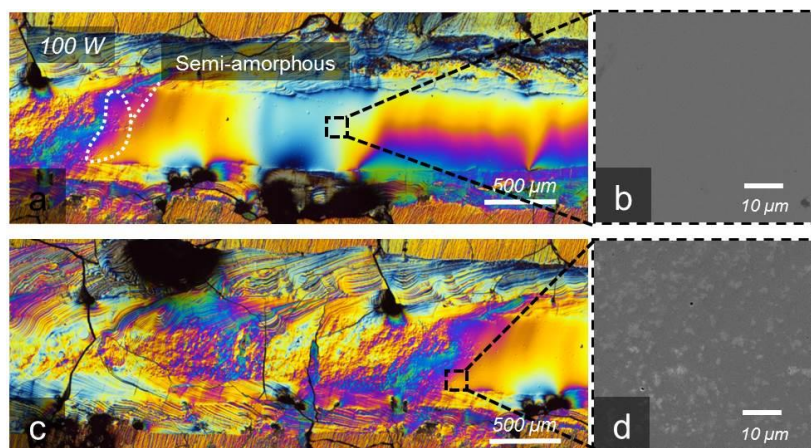
Figure 7. (a) DIC image of a topographically smooth segment of the compositionally graded Cu-Zr deposit and (b) the corresponding secondary electron SEM image of the microstruc-

diameters as small as 40 nm,[17] making it a suitable high-throughput characterization tool for identifying amorphous material in the graded specimens.

Figure 7(a) shows a DIC image of a possible amorphous segment within the line re-melted by the 100 W laser. The surface of the segment was topographically smooth with very few identifiable surface features. In contrast to the smooth segment, the rough and uneven topography of the material to the immediate left of the segment clearly indicated the presence of crystals in this region (Figure 7(c)). To corroborate the DIC results, SEM micrographs of the polished specimen obtained from the middle of the segment appeared featureless (Figure 7(b)), as should be expected from the homogeneous microstructure of metallic glass. Furthermore, an electron micrograph obtained near the end of the smooth segment displayed crystallites of an unidentified phase embedded within a featureless matrix (Figure 7(d)), suggesting a semi-amorphous transition region between the glass and crystalline regions. EDS measurements across this transition region yielded a compositional range of less than 1 at. %. The narrowness of this transition region may reflect the acute sensitivity of GFA to compositional deviations in the binary Cu-Zr system.[16]

ture, from a line re-melted using a laser power of 100 W and travel speed of 16.9 mm/s. The Cu content increases from left to right. (c) DIC image of crystalline material adjacent to the smooth segment. (d) The SEM micrograph recorded from the semi-amorphous region shows crystallites embedded within a featureless matrix.

Electron diffraction in the transmission electron microscope (TEM) was performed to verify the amorphous structure of the material that was identified by DIC.

The TEM sample was prepared by polishing and ion milling a strip of the topographically smooth region from the line re-melted by the 100 W laser. The resulting diffraction pattern featured concentric halos that are characteristic of amorphous materials, validating the reliability of DIC imaging for identifying metallic glass regions in the graded specimens.

An additional compositionally-graded specimen, also prepared using a final re-melt power of 100 W, was used to investigate the glass transition and crystallization behavior of the amorphous region with differential scanning calorimetry (DSC). The region was mechanically separated from the substrate and heated at a rate of 20 K/s. Figure 8 displays the heating trace for the strip of the featureless material. Although the glass transition was weak, the curve displayed a prominent exothermic crystallization peak, suggesting that the topographically featureless material contained a significant volume fraction of metallic glass. T_g was 755 K, and the onset temperature of the crystallization peak (T_x) was 780 K, consistent with the T_g and T_x of the best reported glass former in the Cu-Zr system, $Cu_{64.5}Zr_{35.5}$.[18]

2.2.2 Identifying the composition with the highest GFA

An important parameter to consider during laser re-melting is the laser line energy λ, a parameter quantifying the instantaneous heat input per unit area by the laser to the target substrate material. It is defined mathematically as $\lambda = P/(vD)$ where P is the (absorbed) laser power, v is the laser travel speed, and D is the diameter of the laser beam on the surface of the substrate, assumed to be independent of laser power and set to 1 mm in our study. In laser deposition experiments with $Zr_{58.5}Cu_{15.6}Ni_{12.8}Al_{10.3}Nb_{2.8}$ powder, an excellent glass former, Sun and Flores observed that for a fixed laser power, reducing λ below a threshold value by increasing the travel speed nearly eliminated crystallization in the heat affected zone (HAZ).[5,19] The same effect of laser travel speed was noticed in laser surface melting experiments of $Cu_{60}Zr_{30}Ti_{10}$ substrates.[20] Additionally, they demonstrated that for a fixed travel speed, decreasing the laser power below a threshold value was necessary for vitrification of the substrate's surface. These observations of maximum laser power and minimum travel speed as criteria for vitrification suggest that a maximum value of λ exists for a given alloy composition (λ_{max}), above which the thermal burden becomes too large to bypass crystallization during the cooling of the melt pool.
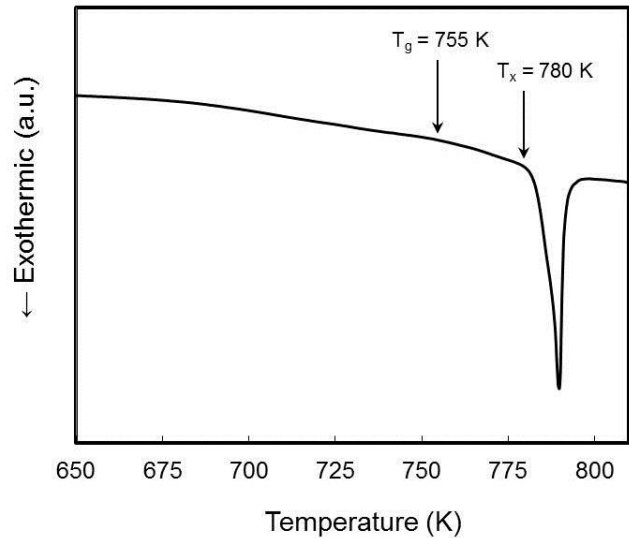

Figure 8. DSC heating trace of the topographically smooth segment mechanically separated from the line re-melted using a laser power of 100 W and travel speed of 16.9 mm/s. DSC data was obtained at a heating rate of 20 K/min.

To investigate the effect of λ on our graded specimen, nine evenly-spaced re-melted lines were made in the direction of the composition gradient, with laser power increasing from 100 to 180 W in steps of 10 W. Figure 9 shows a DIC image of the complete specimen. The observed amorphous segment in each re-melted line is enclosed by dashed lines. The width of the segments deceases with increasing laser power or, equivalently, increasing λ. Although the endpoints of the amorphous segments could not be sharply defined due to the presence of the semi-amorphous transition regions, they were approximated from the DIC image as the positions where the topographically featureless matrix was no longer clearly visible.

The chemical composition at the two endpoints of each amorphous segment was measured by EDS, and the results are plotted versus λ in Figure 10. To achieve statistical precision, each point on the plot represents the average of five measurements at the same position in the specimen. The upper and lower bound data are each well-fitted by linear trend lines. From the intersection of these two lines it may be deduced that the optimum glass forming composition in the graded specimen was $Cu_{64.7}Zr_{35.3}$, in excellent agreement with the composition that has been reported in literature, $Cu_{64.5}Zr_{35.5}$.[16,18] We further deduce that the maximum laser line energy for this optimal composition, above which a glass is not formed, is 10.9 J/mm^2. While this agreement is remarkable, it should be noted that our predicted optimal composition is subject to inherent errors associated with the accuracy of the EDS measurement technique, as well as "operator error" associated with identifying the transition from amorphous (featureless) to crystalline at each endpoint. We estimate that each of these errors contribute ± 1 at. % or less to each measured endpoint and to the predicted optimal composition. If additional precision is required, a more gradual compositional gradient may make the amorphous/crystalline transition more easily discernable, reducing the contribution of "operator error".

The linear narrowing of the range of glassy compositions with increasing laser line energy towards the optimum glass former implies a direct relationship between GFA and λ_{max}. High GFA is reflected in an alloy's ability to carry a larger thermal burden without crystallizing.
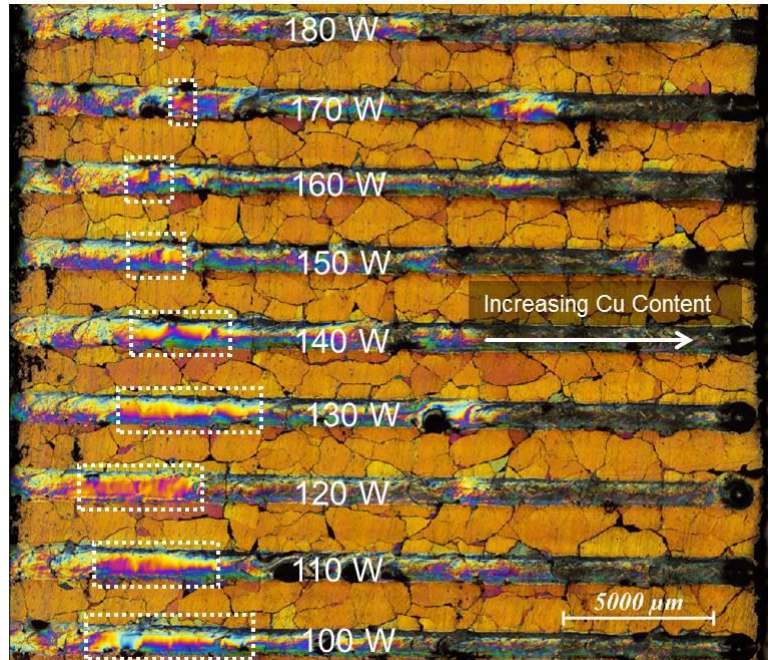

Figure 9. DIC image of a graded Cu-Zr deposit, showing several lines re-melted at different laser powers. The laser travel speed was maintained at 16.9 mm/s. The dashed boxes indicate topographically smooth segments of each line, suggesting that the material is amorphous.
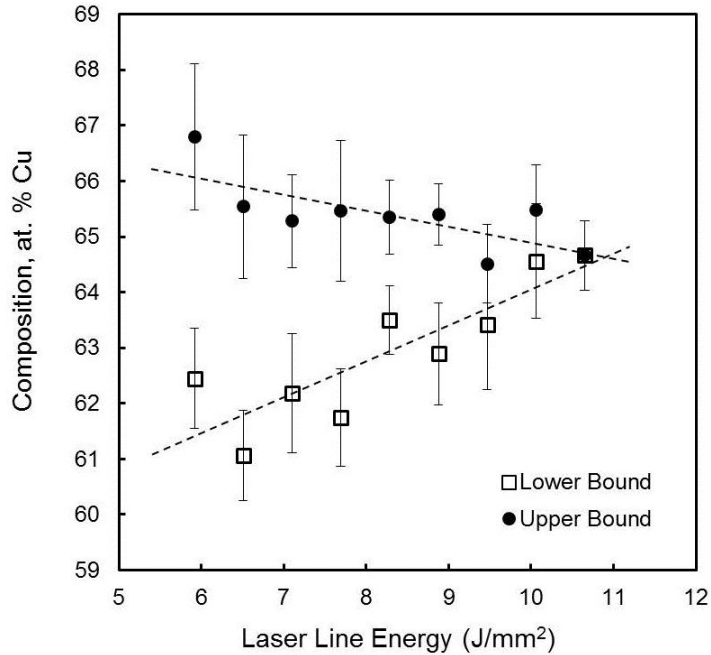
Figure 10. Composition of the graded Cu-Zr deposit at the endpoints of the glassy regions observed via DIC (Figure 4) and SEM, as measured using EDS. As the laser line energy increases, the compositional width of the glassy segment shrinks until only the best glass-forming composition remains.

This ability to isolate and identify the best glass formers within a composition library is a marked advantage of laser deposition over other combinatorial techniques such as sputtering. While smooth composition profiles could be obtained by magnetron sputtering, the exceptionally high quench rate of sputtering, and the resulting ease with which an amorphous structure is formed over a broad composition range, makes it impossible to directly differentiate one composition from another with respect to GFA without relying on "predictive" parameters such as T_{rg}.[15,21]

2.2.3 Identifying additional Cu-Zr glass formers

In addition to $Cu_{64.5}Zr_{35.5}$, several other compositions in the Cu-Zr system have been widely recognized as bulk glass formers with critical casting thicknesses exceeding 1 mm.[22,23] Li and co-workers casted a series of fifteen Cu-Zr wedges ranging 46-70 at. % Cu and identified three "GFA peaks" corresponding to $Cu_{64}Zr_{36}$, $Cu_{56}Zr_{44}$, and $Cu_{50}Zr_{50}$.[15] Although our combinatorial methodology demonstrated the accurate identification of the optimum glass former in the binary system, complete validation of the method would necessitate the ability to identify all other notable glass formers as well. To thoroughly investigate GFA in the Cu-Zr system, we fabricated continuously graded specimens with an expanded composition range.

The new specimen was synthesized according the experimental procedure that was previously described for the original graded specimen. However, during deposition, the range of powder delivery rate for both feedstock powders was expanded to widen the composition range of the finished specimen: 1.78 - 5.24 g/min and 3.91 - 2.29 g/min for the Cu and Zr powders respectively. To adjust for the lower GFA of the other glass formers, the laser powers for the final re-melt was reduced to range from 50 to 90 W, with increments of 5 W for each re-melted line. Another identical specimen was also fabricated, albeit with laser powers ranging from 50 to 130 W, in steps of 10 W. Figure 11 provides a DIC image of one of the completed specimens.

Using the described method for deducing the best glass formers, an additional GFA peak located at $Cu_{50.2}Zr_{49.8}$ was identified in the extended range specimens. Figure 12(a) is a plot of the combined data for the original specimen as well as both extended range specimens.
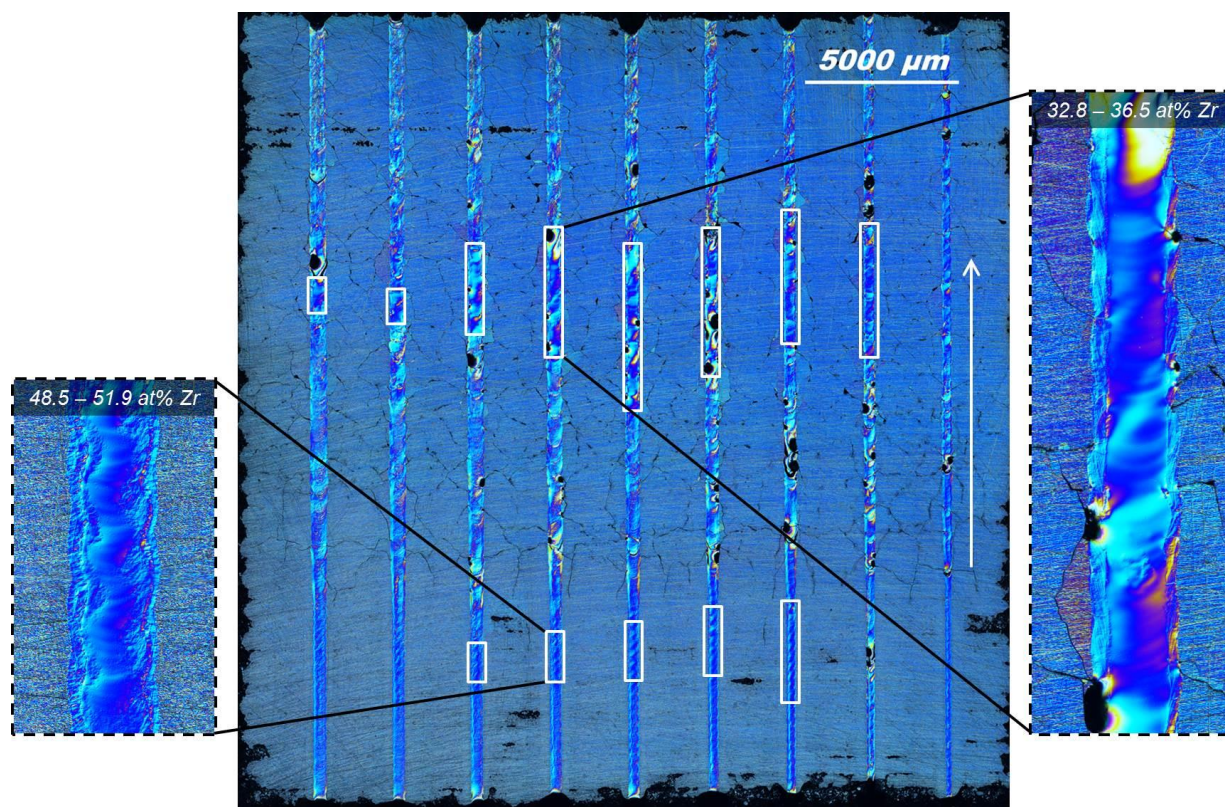
14

Figure 11. DIC image of a graded Cu-Zr specimen with an extended composition range. The re-melted lines in image correspond to nine different laser powers, ranging 50 – 90 W, in steps of 5 W and decreasing from left to right. The boxed-in areas are topographically smooth segments observed in the re-melted lines. These segments correspond to two GFA peaks in the Cu-Zr binary system.
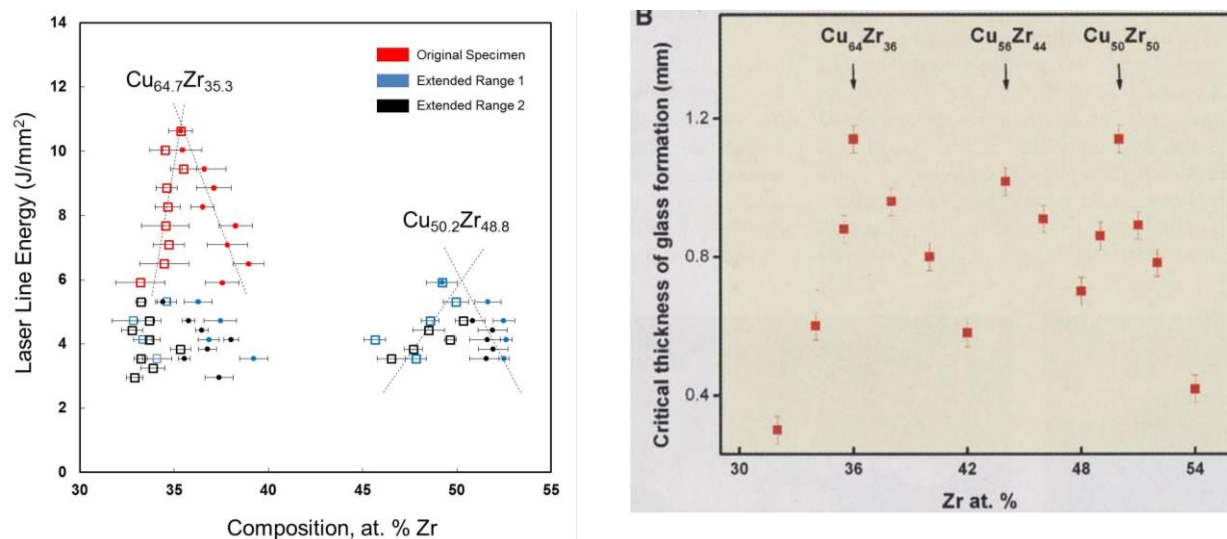

Figure 12. (a, left) Composition of the graded Cu-Zr deposit at the endpoints of the glassy regions observed via DIC (Figure 8) and SEM, as measured using EDS. An additional GFA peak

was observed at $Cu_{50.2}Zr_{48.8}$. The overall results, agree well with wedge casting experiments performed by Li *et al.*[15] (b, right) Plot of critical casting thickness of Cu-Zr binary alloys. Image is taken from Ref. 15.

For comparison, Figure 12(b) shows the GFA plot from Li *et al.*'s wedge casting experiments. The extrapolated peaks line up nearly perfectly with two of the three peaks reported by the authors but the peak at $Cu_{56}Zr_{44}$ was not observed at all in the graded specimens.

A factor inherent to the laser experimental procedure could account for the discrepancy. According to the sequence of fabrication steps, vitrification occurs during the final re-melting step, when both a faster travel speed and reduced laser powers are applied to increase the subsequent cooling rate within the melt pool. Prior to this final step, the deposit is fully crystalline, and depending on the kinetics of melting, certain crystalline phase(s) may not fully melt at low laser powers, leaving behind residual nuclei that could promote subsequent heterogeneous crystallization events.

TEM samples from the center and edges of the glass forming segments in the extended range specimens are currently being prepared via the focused ion beam for selected area diffraction. The structural analysis will confirm the glassiness of the smooth regions and shed light regarding the role and effect of competing crystalline phases on GFA.

2.3 Continuously-Graded Cu-Zr-Ti Compositional Libraries

Following the successful work exploring glass formation in the binary Cu-Zr system, we extended the methodology to investigate the ternary Cu-Zr-Ti system. It is known that minor alloying of Cu-Zr alloys with Ti and/or Al could vastly improve the GFA and enhance mechanical properties[45–49]. Although speculation exists as to the physical reasons minor alloy additions of certain elements improve GFA and mechanical properties of BMGs, the proposed reasons are mostly qualitative and do not provide a reliable means of predicting the specific effect of a minor alloying element in an arbitrary MG alloy.

2.3.1 Fabrication of continuously graded Cu-Zr-Ti specimens by LD

An alternative fabrication scheme was used for the compositionally graded Cu-Zr-Ti ternary specimens. Instead of co-depositing the Cu and Zr powders with varying powder delivery rates, three graded layers of Zr, Cu, and Ti were successively deposited one on top of the other in a 25.4 x 25.4 mm square geometry. The underlying substrate was the same material as before, grade 702 zirconium ground with 320 grit SiC paper and cleaned with methanol to remove surface contaminants. The minimum purities of the powders were 99.9, 99.2, and 99.2 at. % for Cu, Zr, and Ti respectively.

To achieve the graded effect for a single layer deposit, the powder delivery rate was fixed at a constant value and the laser travel speed was varied stepwise from hatch to hatch. For the initial layer, Zr powder was deposited with a 250 W laser, and the travel speed was ramped up from 8.5 to 29.6 mm/s. Next, Cu powder was deposited with a 250 W laser on top of the first layer, following the same tool path. However, the travel speed was *ramped down* from 29.6 to 8.5 mm/s, resulting in the specimen being Zr-rich on one end and Cu-rich on the other. The Cu and Zr powder delivery rates were fixed at 4.20 and 2.83 g/min respectively.

Following the two deposits, nine evenly-spaced, re-melted lines were drawn across the specimen with a 200 W laser traveling at 12.2 mm/s. The re-melting step was necessary to facilitate adequate mixing of the two components. However, whereas the re-melted lines in the binary Cu-Zr specimen were drawn parallel to the direction of the composition gradient, the re-

melted lines in the case of the ternary specimen were created perpendicular to the Cu-Zr composition gradient. The aim for the change in deposition direction was for each of the re-melted lines to hold a constant Cu:Zr molar ratio.

The final fabrication step was to integrate a Ti concentration gradient into each of the re-melted lines. This was accomplished by depositing a layer of Ti in the same manner as with the previous two layers, but using a laser tool path that has been rotated by ninety degrees. The powder delivery rate was fixed at 0.85 g/min; the travel speed was incrementally changed from 8.5 to 29.6 mm/s; and the laser power was set to 150 W. After completion of the third layer, the nine re-melted lines were re-melted again with a 200 W laser traveling at 12.7 mm/s to thoroughly mix the Ti into the alloyed lines. A final re-melt of the 9 lines with a 150 W laser traveling at a faster speed of 16.9 mm/s was performed to encourage vitrification of bulk glass formers within the graded specimen.
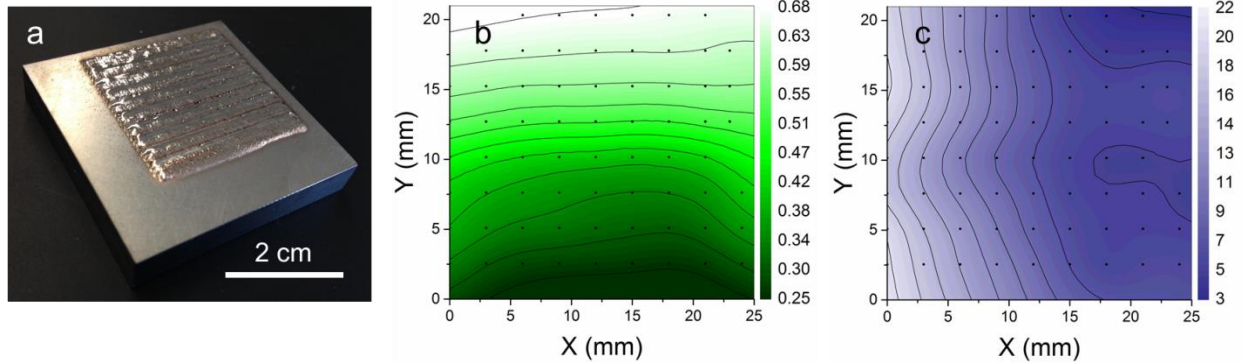

Figure 13. (a) Photograph of the complete ternary specimen. (b) Profile of the $X_{Cu}/(X_{Cu}+X_{Zr})$ ($X = atomic fraction$) molar ratio in the compositionally graded Cu-Zr-Ti ternary specimen. (c) Ti content in the same ternary specimen. The smooth contour fits demonstrate the ability of the fabrication scheme to systematically probe large regions of ternary composition space.
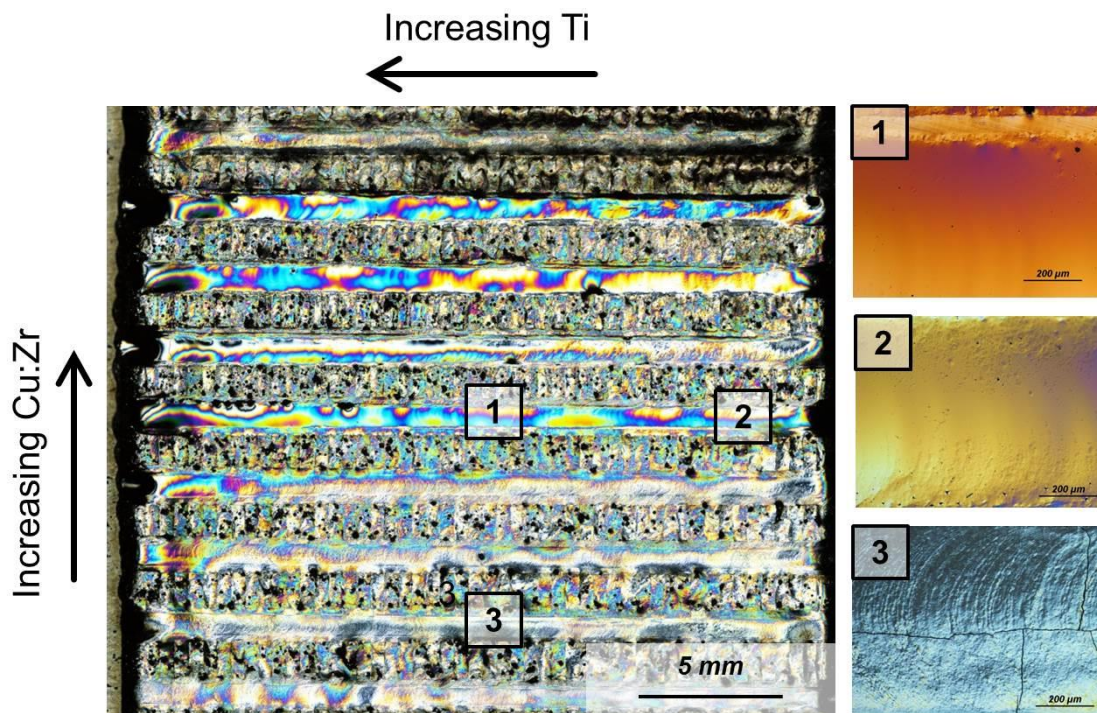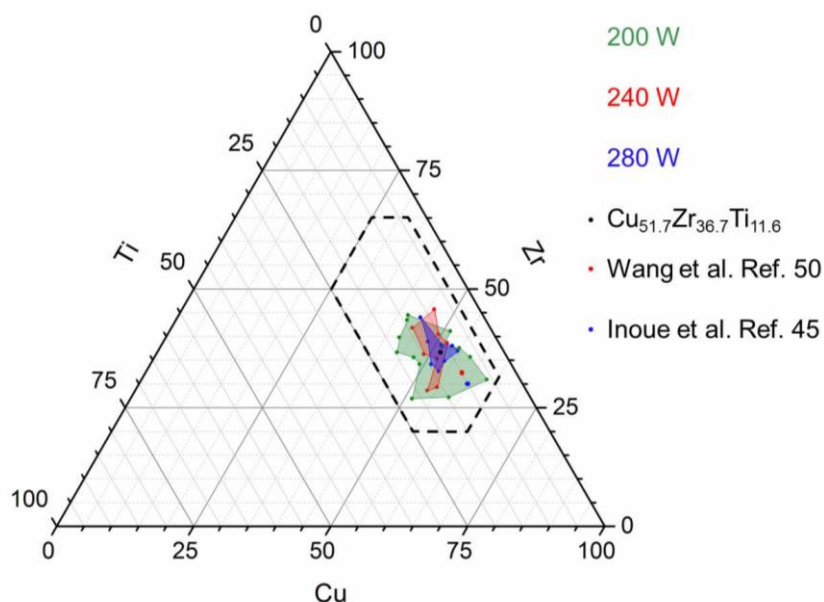
Figure 14. DIC image of the compositionally graded Cu-Zr-Ti specimen. Three topographically distinct regions are marked, with their corresponding microstructures shown to the right of the large image. Regions 1, 2, and 3 are believed to be amorphous, semi-amorphous, and crystalline, respectively.

Composition measurements were recorded by EDS across the specimen to assess the continuity and smoothness of the chemical gradation. Figures 13b and 13c show plots of the $X_{Cu}/(X_{Cu}+X_{Zr})$ (*X = atomic fraction*) molar ratio and Ti content as a function of position. Both sets of data were well-fitted with smooth contours, with the direction of the surface slope indicating that the desired two-dimensional gradation had been successfully fabricated according to the intended design. The DIC image of the unpolished specimen is shown in Figure 14. Again, topographically smooth regions in the re-melted lines were easily distinguished from the rough surface terrain of the crystalline regions. Consistent with the reported improvement of GFA by the addition of Ti, the featureless regions in the ternary specimen appeared to be significantly more prevalent than in the graded binary samples.

2.3.2 Identifying compositional regions of high GFA in the Cu-Zr-Ti system

The strategy of applying higher laser powers stepwise to narrow the range of glass formation was applied to deduce the best glass formers in the graded ternary specimen. However, contrary to the Cu-Zr specimens that featured a one-dimensional gradation, the compositional gradient in the Cu-Zr-Ti specimen was two-dimensional, with every position on the specimen representing a different composition. Therefore, our experimental method of obtaining the best glass formers required the fabrication of multiple specimens, each processed with a different laser power and hence heat input during the final re-melting step.

18

0
100
25
75
Ti 50
Zr 50
75
25
100
0
0   25   50   75   100
Cu

200 W
240 W
280 W

• $Cu_{51.7}Zr_{36.7}Ti_{11.6}$
• Wang et al. Ref. 50
• Inoue et al. Ref. 45

Three ternary composition libraries were produced according to the described deposition scheme. The processing parameters corresponding to each specimen are specified in Table 3.

Table 3 Processing parameters for the laser-processed Cu-Zr-Ti composition libraries.

Library	Powder delivery rate (g/min)			Laser travel speed (mm/s)	Final laser power (W)
	Cu	Zr	Ti		
1	4.12	2.83	0.93	8.47 - 29.63	200
2	4.12	2.83	1.3	8.47 - 29.63	240
3	4.12	2.83	1.51	8.47 - 29.63	280

Measurement of the complete compositional profile via EDS for the three libraries was deemed unnecessary since we had already demonstrated that the original specimen possessed the desired composition gradients. Instead, the approximate boundary positions of the topographically featureless segments were identified by DIC imaging, and the compositions corresponding to the endpoints were measured by EDS to determine the approximate locations of amorphous regions in the Cu-Zr-Ti composition map.

The compositional extent of glass formation in each of the three libraries was defined by plotting and connecting the endpoint compositions to form enclosed regions on the Cu-Zr-Ti ternary map. For statistical precision, each endpoint composition on the plot represents the average of six measurements at the same position. Figure 15 shows the glass forming region of all three specimens on a master plot. The area outlined by a dashed line is the overall composition space that was explored. Similar to the trend observed in the graded binary samples, it is evident that the amorphous region diminishes with increasing laser power or laser line energy. Based upon the trend, the best glass-former within the explored composition space was estimated to be $Cu_{51.7}Zr_{36.7}Ti_{11.6}$, represented by the black dot in the figure. In comparison, the best reported glass former reported by Wang *et al.* is $Cu_{57.6}Zr_{32.4}Ti_{10}$, with a reported casting thickness of 4 mm.[13] Inoue *et al.* also explored glass formation in the Cu-Zr-Ti ternary system by casting and melt-spinning a series of $Cu_{60}Zr_{40-x}Ti_x$ (x = 0 – 40) alloys.[14] $Cu_{60}Zr_{30}Ti_{10}$ was determined as the best glass former in the series, also with a maximum casting thickness of 4 mm.

19

Figure 15. A plot showing the GFA of Cu-Zr-Ti alloys within the compositional region enclosed by the dashed line. $Cu_{51.7}Zr_{36.7}Ti_{11.6}$ was deduced to be the optimum glass former. For comparison, the red and blue single dot indicate compositions reported by Wang *et al.*[13] and Inoue *et al.*[14] as the best glass formers in the ternary system.

Several factors may explain the discrepancy between the predicted and reported best glass formers. First of all, unlike the graded binary Cu-Zr specimens, the semi-amorphous transition regions of a few re-melted lines spanned a range of clearly more than a few atomic percent, presenting a greater challenge in resolving the endpoint compositions of the featureless segments. Greater operator errors in composition measurement would likely adversely affect the accuracy of prediction. It is also very possible that the reported compositions, $Cu_{57.6}Zr_{32.4}Ti_{10}$ and $Cu_{60}Zr_{30}Ti_{10}$, are not actually the best glass formers. Inoue and collaborators had casted their alloys in large stepwise increments of 5 at. %; it is plausible that better glass formers in the series were entirely missed, given the acute sensitivity of glass forming ability to changes in composition. The compositional region, with a fixed copper content, was also too narrow to draw definite conclusions regarding GFA in the system. Wang *et al.*'s results were more convincing, considering that multiple series of Cu-Zr-Ti alloys along constant Cu_x-Zr_{100-x} tie lines were interrogated.[13] However, the ternary tie lines were not evenly spaced, with large compositional gaps between them, raising doubts regarding the validity of their results.

To validate our method for optimizing GFA, discrete wedge samples of $Cu_{51.7}Zr_{36.7}Ti_{11.6}$, $Cu_{60}Zr_{30}Ti_{10}$, and $(Cu_{0.64}Zr_{0.36})_{90}Ti_{10}$ were prepared by copper mold suction casting. Care was taken to maintain consistent processing conditions for all three alloys. The wedge critical casting thickness measured by optical microscopy was 1.5, 1.2, and 1.35 mm respectively for $Cu_{51.7}Zr_{36.7}Ti_{11.6}$, $Cu_{60}Zr_{30}Ti_{10}$, and $(Cu_{0.64}Zr_{0.36})_{90}Ti_{10}$, confirming the expected ranking of GFA among the three alloys.

Figure 16 provides differential scanning calorimetry (DSC) heating traces of the three suction cast samples. The glass transition temperature (T_g), crystallization temperature (T_x), and liquidus temperature (T_l) for each alloy are listed in Table 2. Also listed are $T_{rg} = T_g/T_l$ and $\Delta T = (T_x - T_g)$, the two most prevalent temperature-based indicators of GFA. It is noteworthy that neither parameter accurately predicts the ranking of GFA among the three alloys. According to ΔT, $Cu_{51.7}Zr_{36.7}Ti_{11.6}$ is the poorest glass former. On the other hand, the similar T_{rg} among the alloys incorrectly suggests that no differences exist in their glass forming ability. These results bring to reminder the unreliability of existing temperature-based predictors. While characteristic temperatures may reflect certain crucial aspects of glass formation, they could not possibly embody all the thermodynamic and kinetic factors that determine an alloy's ability to vitrify.

Table 4 Characteristic temperatures and temperature-based predictive parameters of three Cu-Zr-Ti metallic glass alloys.

Alloy Composition	T_g (K)	T_x (K)	T_l (K)	T_{rg}	ΔT (K)
$Cu_{60}Zr_{30}Ti_{10}$	708	751	1146	0.62	43
$(Cu_{0.64}Zr_{0.36})_{90}Ti_{10}$	693	740	1167	0.59	47
$Cu_{51.7}Zr_{36.7}Ti_{11.6}$	682	715	1146	0.60	33

2.4. High throughput mechanical properties assessment and optimization by nanoindentation and dynamic modulus mapping

Although boasting superior mechanical properties such as tensile yield strengths exceeding 1 GPa and the ability to undergo large elastic deflections compared to conventional alloys, monolithic BMGs generally suffer from a lack of macroscopic ductility in unconfined loading geometries such as uniaxial tension, preventing their application as structural materials.[24,25]

While crystalline alloys derive their ductility and toughness from the abundance and mobility of dislocation defects, BMGs on the other hand, due to the complete absence of dislocations, cannot accommodate homogenous plastic deformation. Instead, plastic strain has been shown to accumulate in the form of localized shear bands that are approximately aligned with the plane of maximum resolved shear stress.[26,27] When placed under uniaxial tension and loaded to failure, monolithic BMGs typically exhibit the growth of a single dominant shear band towards apparent brittle fracture.[24,28,29,30] However, despite their general reputation as brittle materials compared to work-hardenable engineering alloys, intrinsically "tough" Pd-based and Zr-Cu-Al-based BMGs with surprisingly high resistance to fracture have recently been discovered,[27,31,32] prompting the search for other monolithic BMGs with high toughness.

The origins of toughness in monolithic BMG alloys are not yet fully understood, but several empirical criteria based on elastic constants have been established. More specifically, BMG toughness has been directly related to a high Poisson's ratio (v) or equivalently, a low ratio of shear modulus to bulk modulus (μ/B).[33,34] By plotting the fracture energy versus v and μ/B for a series of metallic glass alloys, Lewandowski *et al.* showed that intrinsically tough BMGs must possess $v > 0.31$-0.32 and $\mu/B < 0.41$-0.43 (Figure 12).[33]

Elastic constants alone, however, could not provide a universal benchmark for comparing toughness between alloys. For example, while it is likely that an alloy with $v = 0.4$ has higher fracture toughness than another alloy with $v = 0.2$, two alloys with identical v are not necessarily equally tough. This is not surprising, as resistance to fracture is ultimately dictated by the mechanisms of plastic, not elastic, deformation that occur ahead of the crack tip. To illustrate, in 2011 researchers at the California Institute of Technology reported a damage-tolerant Pd-based BMG that displayed high fracture toughness values previously unobserved in metallic glasses.[27] The plastic zone size in fracture toughness tests was estimated to have a radius as large as 6 mm and contained a dense population of shear bands. The multiple shear band activity provided a mechanism for energy dissipation ahead of the crack tip, leading to significant plastic shielding and exceptional fracture toughness.

More recently, Wang *et al.* explored the effect of surface mechanical attrition treatment (SMAT) on the tensile ductility of BMG tensile specimens.[35] Similar to shot peening, the SMAT process involves the repeated collision of steel balls against a specimen surface. The result is a roughened surface with a substantial accumulation of residual compressive stress. When applied to a Zr-based BMG for various durations, profuse shear banding was observed at the surface of the specimens, with longer treatments producing a greater degree
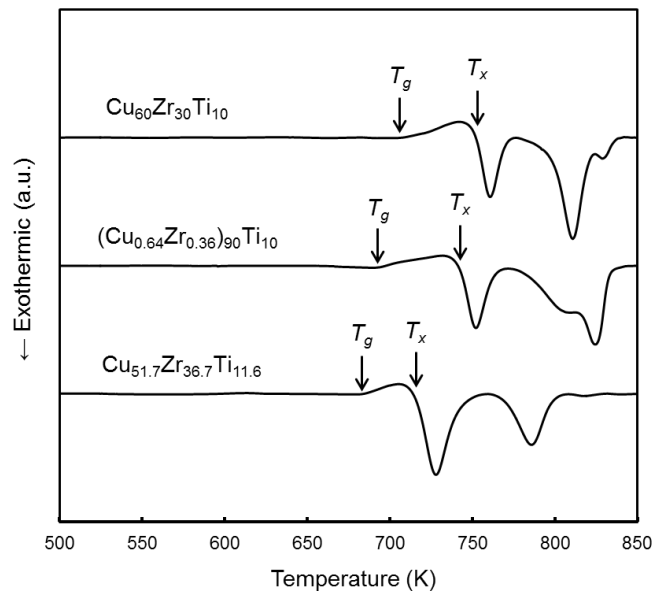

Figure 16. DSC scans of the three suction-cast Cu-Zr-Ti specimens. The scans were performed at a heating rate of 20 K/min.

of shear band activity. Subsequent tensile loading to failure of the specimens showed an increased macroscopic ductility in the loading curves with longer treatment times, indeed up to 4 % plastic strain. In contrast, the untreated specimen exhibited nearly no additional plasticity upon yielding.

These notable examples, among others, emphasize that from a mechanistic point of view, high shear band activity upon yielding of a BMG alloy is favorable in terms of toughness and ductility. In recent years, several experimental and computational studies have suggested a direct link between the population of shear transformation zones (STZs) responsible for the nucleation of shear bands and the intrinsic atomic-scale elastic heterogeneities in monolithic glasses.[36,37] However, like GFA, no known criteria have been suggested that could reliably predict the shear band behavior solely based on the chemical composition of an alloy. To date, assessment of the toughness and ductility of BMG alloys still rely on conventional ASTM test methods, which, while dependable, are incompatible with our combinatorial design approach.

2.4.1 Establishing compositional trends in hardness and modulus

Alternatively, instrumented nanoindentation provides a means to conveniently evaluate the local (nanoscale-microscale) mechanical behavior of a material without the need to fabricate bulk test samples. Unlike more traditional indentation methods, instrumented nanoindentation measures the load-displacement (P-h) response of a material, from which hardness and reduced modulus could be extracted. The hardness is calculated from the max load (P_{max}) and contact depth (h_c) and the reduced modulus is obtained from the slope of the unloading portion of the curve.[38] Deng and collaborators used instrumented nanoindentation as a combinatorial tool to explore the compositional dependence of hardness and elastic modulus on a sputtered Zr-Cu-Al metallic glass thin film library.[39] We have adopted a similar strategy for our laser-deposited graded specimens.

In contrast to the GFA study, a high-throughput investigation of the mechanical properties by nanoindentation would benefit from composition libraries that feature distinct, isolated compositions. Although lattice mismatch resulting in localized stresses and strains are usually discussed in the context of structurally disparate crystalline materials, similar effects could be present in the continuously-graded amorphous specimens. As the glass microstructure varies across the compositional profile of the specimens, the resulting atomic-level strains and corresponding stresses could be manifested as artifacts in the measured reduced modulus and hardness values.

To achieve compositional isolation, Cu-Zr-Ti compositional libraries were fabricated as a square, 12 x 12 array of discrete dots, each dot featuring a fixed chemistry (Figure 17). The dots were spaced 2 mm apart. In the first step of the deposition process, Cu and Zr powder were continuously fed, and the stage followed a horizontal raster toolpath from the top left corner of the array to the bottom right corner. To deposit the hemispherical dots, a 250 W laser was pulsed at each of the 144 positions for 120 milliseconds. The balance of copper and zirconium powders was adjusted from row to row such that a Cu-Zr composition gradient was achieved along each vertical column in the array while remaining approximately fixed across a horizontal row. After the initial deposit, each dot was re-pulsed with a 200 W laser for 200 milliseconds. Ti was then deposited with a 150 W laser over the entire area of the initial deposit, with the travel speed increasing from right to left to create a graded Ti profile in the horizontal direction. The Cu-Zr-Ti dots were re-pulsed with a 200 W laser to homogenize the compositions and pulsed a final time with a 180 W laser for a short duration of 60 milliseconds to promote glass formation.
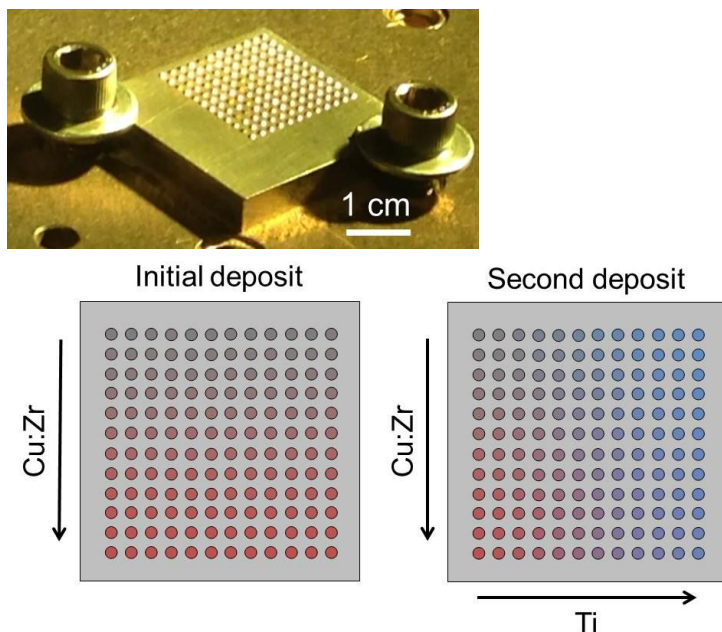
Figure 17. (a, top) Photograph of the Cu-Zr-Ti discrete dot composition library. (b, bottom) Schematic illustrating the deposition process. Arrows indicate direction of increase.

Similar to the continuously graded libraries, the vitrified dots featured a liquid-like, smooth surface that could be easily distinguished from the rough topography of the crystallized dots (Figure 18). Of the 144 dots, 92 were identified as amorphous. Scanning probe microscopy of the vitrified dots yielded sub-nanometer surface roughness values that were substantially superior to mechanically polished surfaces. Furthermore, because the apex of a hemisphere is flat, instrumented nanoindentation could be performed directly at the center of each dot without requiring further specimen preparation.

To establish compositional trends in the mechanical properties of Cu-Zr-Ti glasses, instrumented nano-indentation was carried out across ea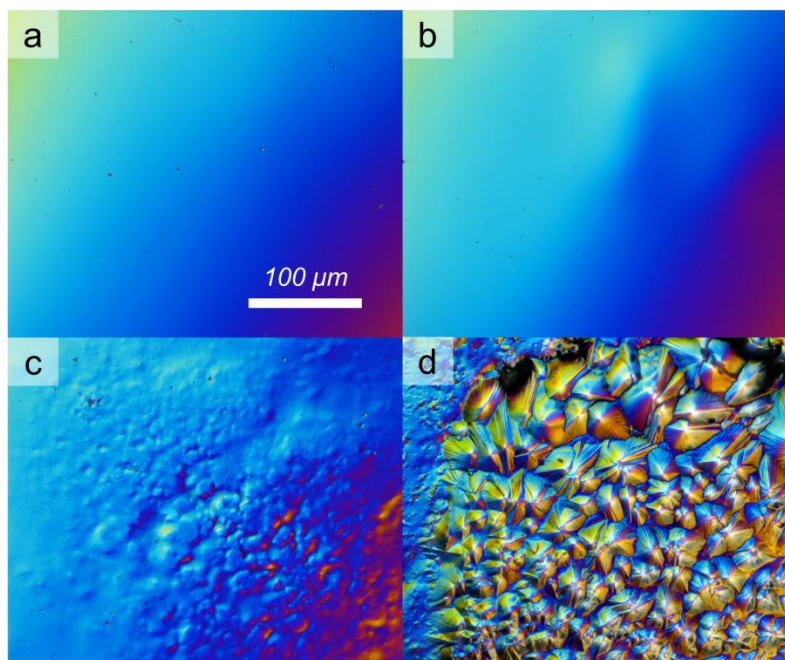ch of the 92 compositions in the array. Four quasi-static indents were performed at the center of each dot in a fully automated test sequence. All of the high-throughput mechanical testing was accomplished with a Hysitron™ TI 950 nanoindenter, equipped with a diamond Berkovich tip.

Figure 19 shows property-composition maps of the measured reduced modulus and hardness values. Each point on the maps represents the averaged value of the four separate indents. The fitted contours displayed smooth compositional trends, providing a pallet of mechanical properties whereby alloys could be selected for specific engineering applications. The compositional trends in hardness and modulus also provide a means to further understand structure-property correlations. In general, the mechanical properties of metallic glass alloys are functions of their chemical

Figure 18. DIC optical micrographs showing the various surface topographies in the as-deposited ternary dot libraries. (a–b), amorphous (c) semi-amorphous, and (d) crystalline.

bonding character and the topological arrangement of the atomic species. Therefore, compositions corresponding to local maxima in the property maps potentially indicate outstanding characteristics of the structure, for example a higher degree of dense atomic packing or a stiffer elastic backbone.
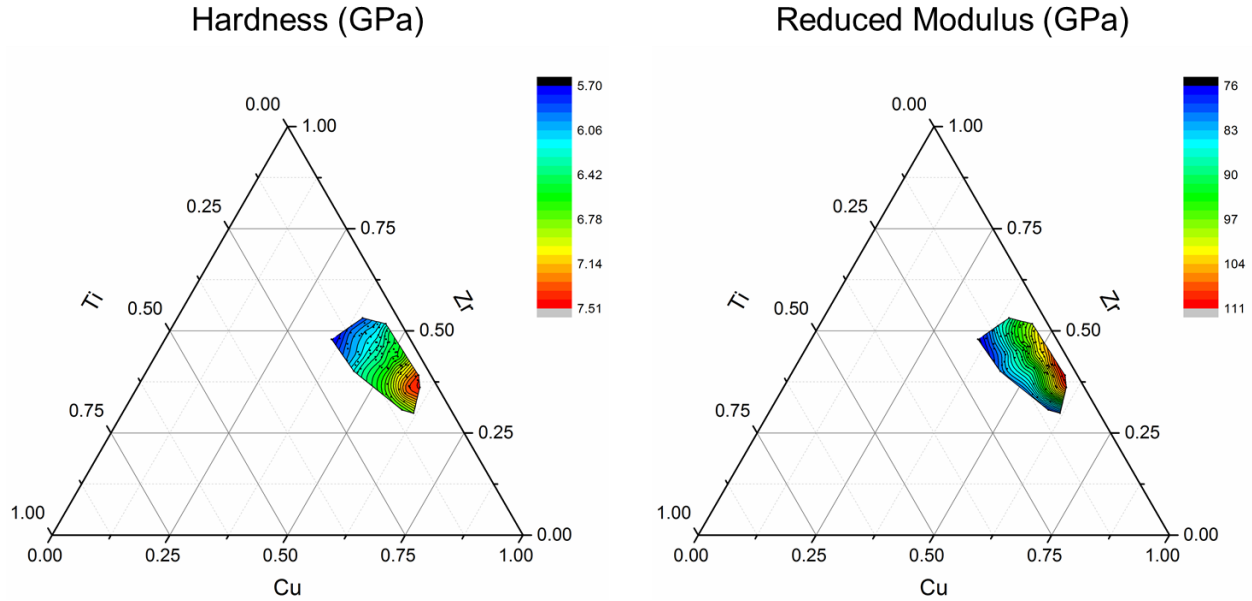

Figure 19. Hardness and reduced modulus values plotted on ternary Cu-Zr-Ti composition maps. The values were collected via instrumented nanoindentation measurements performed on the discrete dot composition libraries.

2.4.2 Dynamic modulus mapping of monolithic BMG alloys

In recent years, a number of computational and experimental studies have convincingly demonstrated the spatially heterogeneous structure inherent to amorphous materials and the implications of structural heterogeneity on the mechanical behavior of MGs.[36,37,40-44] Egami et al. reported that as much as 25 % of the volume in MG alloys is composed of liquid-like anelastic configurations.[40] Similarly, a notable molecular dynamics study on a model $Cu_{64}Zr_{36}$ alloy identified geometrically unfavorable soft spots that exhibited large, non-affine atomic-scale deformations.[37] It has been proposed that these "soft" features are directly associated with shear transformation zones and thus are responsible for the plastic behavior of MG alloys. Although structural heterogeneity has not been directly observed experimentally, its existence is implied in experimental results showing the spatial fluctuation of elastic properties. Samwer et al. used an atomic force microscopy indentation method to probe the elastic modulus of an amorphous Pd-Cu-Si ribbon over a 200 x 200 nm area and compared the histogram of the measured values to a fully devitrified sample.[36] The large Gaussian spread of the data collected from the glassy samples corroborated the existence of structural heterogeneity in real MG alloys, and it was suggested that a locally denser population of non-affine soft spots are responsible for the low end of the measured modulus distribution.

We have used dynamic modulus mapping in the nanoindenter as an alternative method to probe the spatial distribution of elastic properties across the surface of the Cu-Zr-Ti dot specimens. In dynamic modulus mapping, a sinusoidal load function with load amplitude P is applied to the material while a piezoelectric actuator scans the indenter tip over a user-defined area. The dynamic displacement d of the material is measured as well as a phase shift θ. The storage and loss stiffness are then defined as

$$\text{storage stiffness} = \frac{P}{d}\cos q,$$

$$\text{loss stiffness} = \frac{P}{d}\sin q.$$

The stiffness values are easily converted to modulus values by applying Hertzian contact mechanics for a spherical indenter tip. In all our mapping experiments, the frequency of oscillation was set to 200 Hz and the dynamic load amplitudes were chosen to result in a 1-2 nm displacement amplitude. The maps were collected over a 3 x 3 µm scan area on five of the amorphous dots.

Figure 20 provides a compiled montage of the storage modulus maps. For comparison of the statistical spread between different maps, the modulus values are represented as a % deviation from the average modulus. Although the loss modulus maps (not shown) did not exhibit noticeable features, the storage modulus maps clearly contained distinct regions of higher modulus values. From the well-defined boundaries of the stiff features in some of the maps, it is suspected that nanocrystals undetectable by our high-throughput screening method may be embedded within an amorphous matrix. Electron diffraction samples extracted from the center of the dots are currently being prepared to confirm whether the dots are fully amorphous.
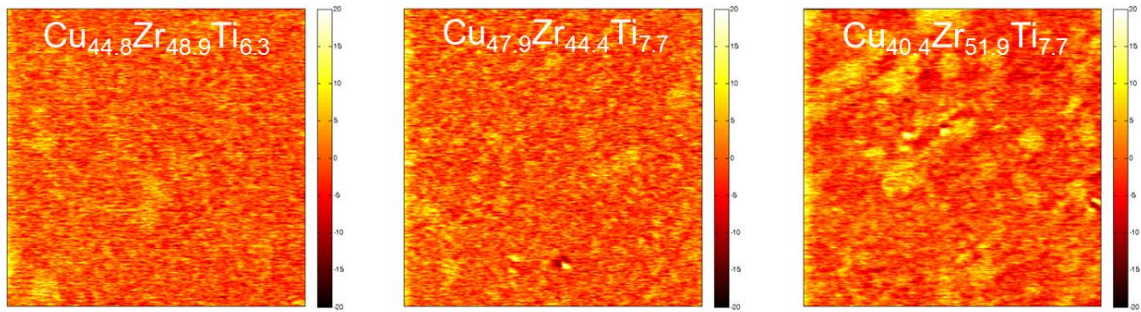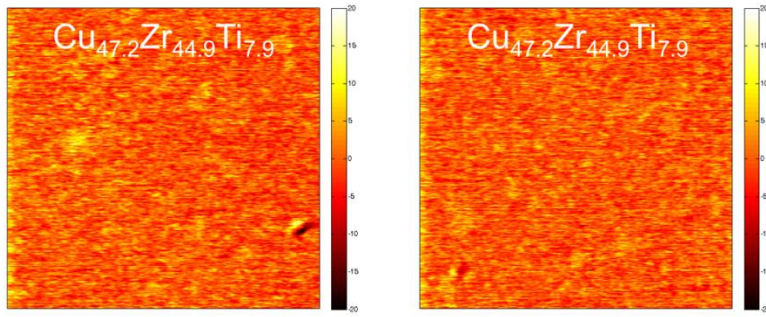
Figure 20. Modulus maps collected from selected dots in the discrete dot Cu-Zr-Ti composition library. For comparison purposes, the values are represented as a % deviation from the norm.

3. EXPLORE POSSIBLE COMPOSITIONS AND COMPOSITION GRADIENTS THROUGH COMPUTATIONS

In order to develop a full design methodology for graded BMG alloys with the desired gradients in mechanical properties, we have developed an atomistic-modeling based design capability in parallel to the experimental efforts in order to be able to form a validated design loop, profiting both from computational speed as well as from experimental validation.

2.1 Summary: Computational design capability for BMGs

In order to engineer kinetic impactors from graded metallic glass, we must first identify systems capable of forming glass, identify compositions able to be graded using LENS or similar technology, and estimate the relevant mechanical properties of the glass. Despite successful development of a few well-understood industrial alloys, identification of glass forming ability *a priori* is largely understood through a set of empirical rules. Using molecular dynamics simulations,[45-47] we have identified a simple and computationally efficient method to describe glass forming ability across an alloy system based on the newly proposed "step-height criterion". This method has been tested for the Cu-Zr and Al-La systems with promising results.

Furthermore, we have demonstrated, as well known from previous work, that MD is also capable of determining relevant mechanical and thermal properties making MD a powerful method for identifying and optimizing metallic glass properties.

Finally, in order to be able to model alloys with many components and arbitrary constituents, we have developed a novel potential fitting approach that allows fitting a sensible potential for an alloy system within a few days. The new method is called Rapid Alloy Method for Producing Accurate General Empirical Potentials" (RAMPAGE) and is freely accessible on our webpage atomistics.osu.edu.

2.2 Computational determination of glass forming ability

In order to examine with molecular dynamics (MD) simulations how easily an alloy can form an amorphous glass, several approaches have been proposed in the past. Using a Voronoi[48] analysis, the local neighborhood of each atom can be tracked as the system transitions from liquid to glass. Atoms in a liquid,[49] and subsequently in a glass, form small clusters of atoms dictated by topological close-packing principles;[50] clusters cannot efficiently fill space,[51] promote amorphous structures and frustrate crystallization. Significant consideration has been given to each atom's immediate surroundings, known as short-range ordering.[52] Relative changes in this local environment can be described in terms of liquid viscosity. The temperature dependence of

26

viscosity is called "fragility" and has been used to investigate glass forming ability in metallic, organic and oxide glasses.[53-55]

As discussed below, packing analyses can sometimes have misleading results, as can be the case for fragility modeling. Within this project, we found that an alternative criterion, which is in addition computationally rather efficient, can give more reliable predictions of GFA. The data presented in Figure 21 shows the fraction of atoms with a coordination number of 12 as a function of temperature. Coordination 12 was chosen because it directly competes with the FCC and HCP crystal structures. Large, steep changes are poor glass formers, while small steps tend to be good glass formers as shown in Figure 21. As shown in Figure 22, the step height may correlate with liquid fragility in Al-La. We peopose that this correlation could hold the key to *a priori*, computation-based determination of glass forming ability.

Determining fragility requires a separate, expensive simulation that can represent half or more of the total computational expense for a given alloy composition. Even after expending this effort, the resulting data can be unreliable, requiring statistical analysis to use in any scientifically rigorous way. Finding the step height requires data already stored as part of the liquid-to-glass quench simulation. If step height could be defin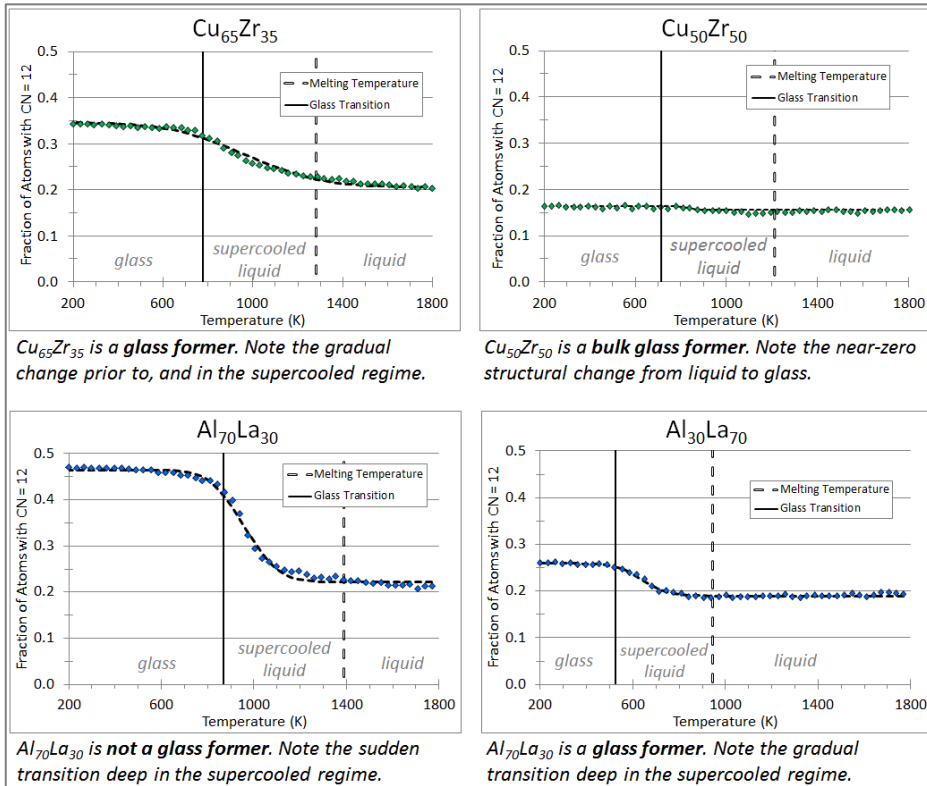itively proven to correlate to fragility, it could reduce the computation time required for each alloy, while eliminating the least reliable data provided by simulations. The experimental determination of fragility requires sensitive measurements on a supercooled liquid[56] or extrapolation of high temperature data to the glass transition. By contrast, an experiment to find the step height would require measurements of the liquid structure at high temperature and the final glass: measurements that have already been made consistently.[57]

$Cu_{65}Zr_{35}$ is a **glass former**. Note the gradual change prior to, and in the supercooled regime.

$Cu_{50}Zr_{50}$ is a **bulk glass former**. Note the near-zero structural change from liquid to glass.

$Al_{70}La_{30}$ is **not a glass former**. Note the sudden transition deep in the supercooled regime.

$Al_{70}La_{30}$ is a **glass former**. Note the gradual transition deep in the supercooled regime.

Figure 21: Fraction of atoms with coordination number 12 as a function of temperature shown for four glass forming simulations: (a) $Cu_{65}Zr_{35}$, (b) $Cu_{50}Zr_{50}$, (c) $Al_{70}La_{30}$, (d) $Al_{30}La_{70}$. Good glass formers (a), (b) and (d), have small step heights and gradual transitions from liquid to glass. Poor glass formers, (c), have tall, sudden steps.

27

Without experimental input, this method can qualitatively rank candidate compositions, and possibly bound the glass forming range. With the inclusion of some experimental data from Ref. 58, separation of compositions capable of forming glass becomes possible. As shown in Figures 22 and 24, no Al-La alloy forms glass when the step height exceeds 0.105. Using this threshold, the gap in glass forming from La_{13} to La_{43} can be successfully filtered. This finding is also consistent with the understanding that high fragility can indicate poor glass forming ability. Such a threshold may exist in Cu-Zr, but the narrow band of fragilities displayed in that system does not provide sufficient resolution to verify it (Fig. 23).
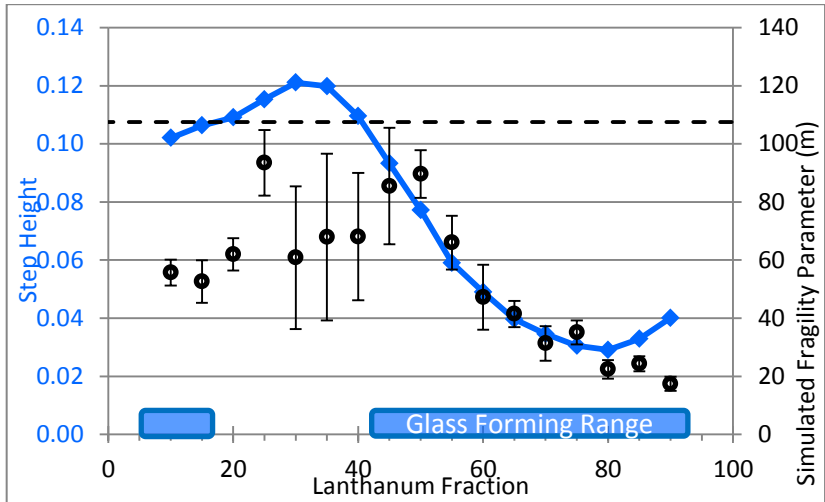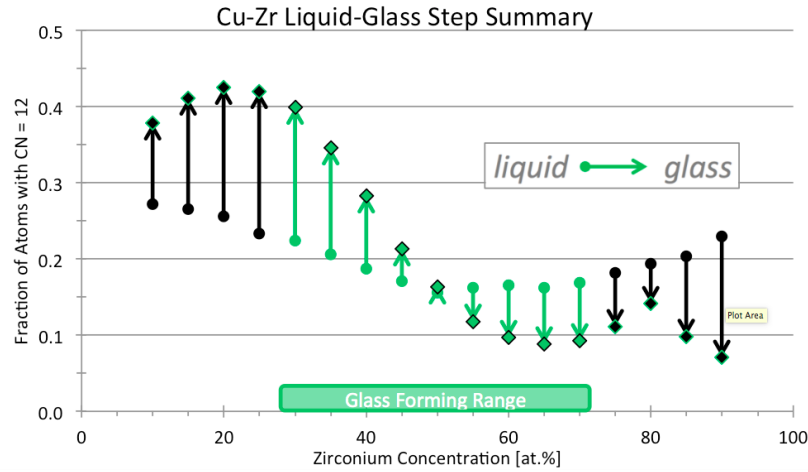

Figure 22: Relationship between liquid fragility and step height for the Al-La glass system. The rough correlation between the two could form the basis for reliable computation-first determination of glass forming ability, as fragility is the best available indicator of experimental glass forming ability. If this relationship holds for other systems, it could eliminate both a computational end experimental trouble-maker.

Figure 23: Step heights for all simulated Cu-Zr compositions. Experimental glass formers are green and experimental non-glass formers are black. The marker indicates the fraction of atoms with coordination number 12 in the liquid, and the arrow points to the concentration of coordination number 12 in the glass. $Cu_{50}Zr_{50}$ had no discernable step height and is also an experimental bulk glass former, capable of forming amorphous sections over 1 cm thick. No threshold in step height filters the glass forming section due to crystallization in the simulation above Zr_{70}.
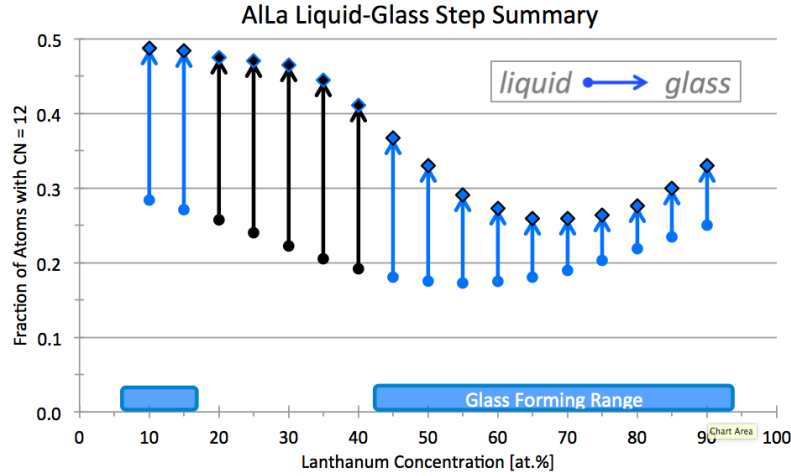

Figure 24: Step heights for all simulated Al-La compositions. Experimental glass formers are blue and experimental non-glass formers are black. The marker indicates the fraction of atoms with coordination number 12 in the liquid, and the arrow points to the concentration of coordination number 12 in the glass. Al-La is unique in that two discrete glass forming ranges exist with a gap spanning La_{17} to La_{43}. This gap can be successfully filtered as shown in Figure 22. The existence of the gap would likely preclude grading for compositions near its ends.

2.3 RAMPAGE interatomic potentials

The step-height method proposed in Sec. 2.2 shows promise for binary alloys, but the most deployable metallic glasses have 3 or more components. In order to simulate these complex systems with MD requires matching interatomic potentials. Multi-component potentials can be produced, but always trade accuracy for ease of production. The easiest method, the Johnson Alloy Model (JAM),[59] linearly interpolates the elemental potentials according to the electron density term. This method is exceptionally efficient but has been shown to cause unphysical results, particularly in amorphous systems. The traditional method of creating highly accurate potentials takes a holistic view of the system and aims to incorporate as many test structures as possible.[60] A single potential can take months or years to generate with this approach.

In order to test many metallic glass alloys, a tool was created to produce potentials superior to the JAM, but with substantial automation over the traditional method. The "Rapid Alloy Method for Producing Accurate General Empirical Potentials" (RAMPAGE) was developed to

quickly fit multi-component Finnis-Sinclair-type EAM potentials from DFT and experimental data. Using this tool, the glass-forming method previously described could be extended to actual engineering applications in metallic glass. Creating and supporting this tool has required

As an impactor penetrates a medium, it encounters significant friction and substantial heating. Critical metallic glass properties, like viscosity and density, change rapidly as temperatures approach and exceed the glass transition temperature (T_g). Increases in temperature can lead to crystallization, melting or complete destruction of the glass. Therefore, thermal properties and the expected change in mechanical properties should be considered for impactor design. MD simulations track changes in viscosity of the glass with temperature and the glass transition temperature can be found with reasonable experimental agreement as shown in Figures 25 and 27 for CuZr, and Figures 26 and 28 for AlLa. MD employs a very fast quench rate, slightly elevating the simulated glass transition temperature.[61,62] Coupled with FEM calculations, this information can determine the ideal dimensions to ensure a payload will survive to a particular depth.
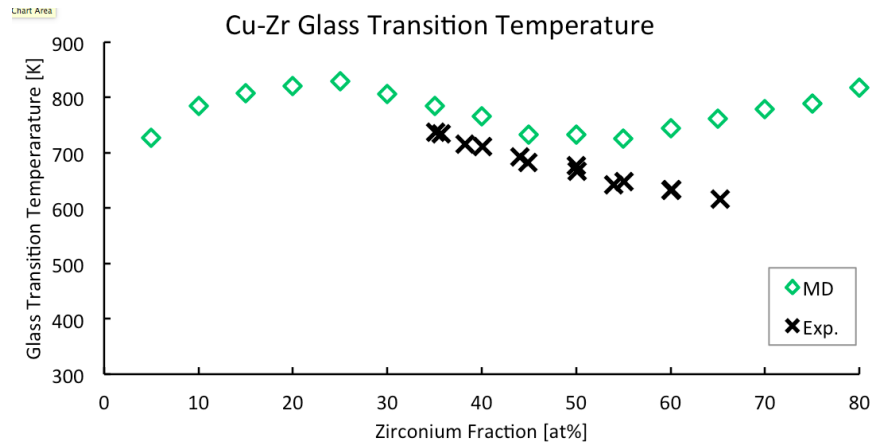

Figure 25: Simulated and experimental glass transition temperatures for Cu-Zr metallic glass alloys. Experimental data from Refs. 63 and 64.
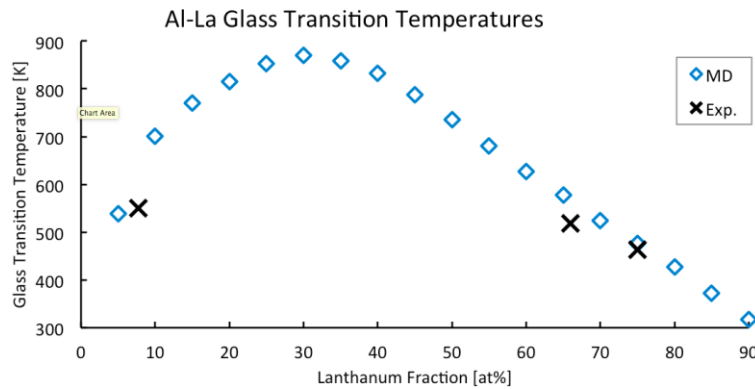

Figure 26: Simulated and experimental glass transition temperatures for Al-La metallic glass alloys. Experimental data from Ref. 66.
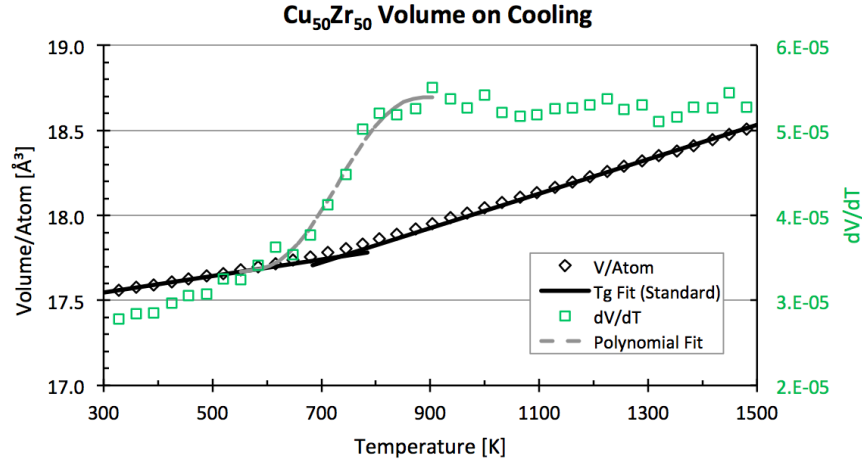
30

Figure 27: Volume per atom as a function of temperature. The change in volume with temperature (dV/dT) is fit to a polynomial. The derivative of the polynomial maximizes at the glass transition temperature. As an impactor heats due to friction, changes in volume per atom will affect density and strength which were found to be primary design criteria. Simulations can determine the maximum operating temperature for a given alloy and provide the dependence of density on temperature.
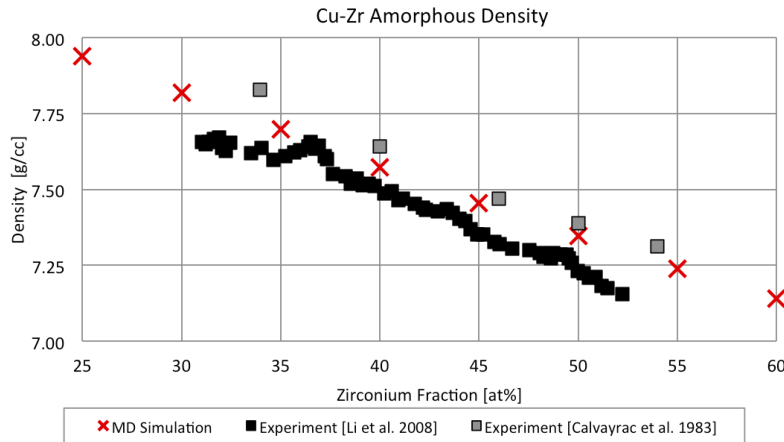

Figure 28: Experimental and simulated mass density for Cu-Zr. Experimental data from Refs. 67 and 68.

2.4 Computational prediction of metallic-glass properties

Molecular dynamics provides other necessary design information. As shown in Figure 28, MD reproduces the mass density of Cu-Zr metallic glass very well. As the FEM results indicate that density is a powerful design parameter this makes MD a powerful tool for identifying metallic glasses best suited to impactor applications.

Molecular dynamics can provide qualitative estimates of a material's yield strength from simulated stress-strain curves as shown in Figure 29. Due to the high strain rates simulated in MD, the simulated yield strength and T_g are overestimated but compositional trends and system-wide behaviors are preserved.[69,70] The same simulation that provides yield data also provides the moduli. Coupled with FEM predictions discussed in Sec. 1, these additional design

31

parameters extracted from MD simulations can be used to optimize impactor materials design, validated by the experiments described in Sec. 2.
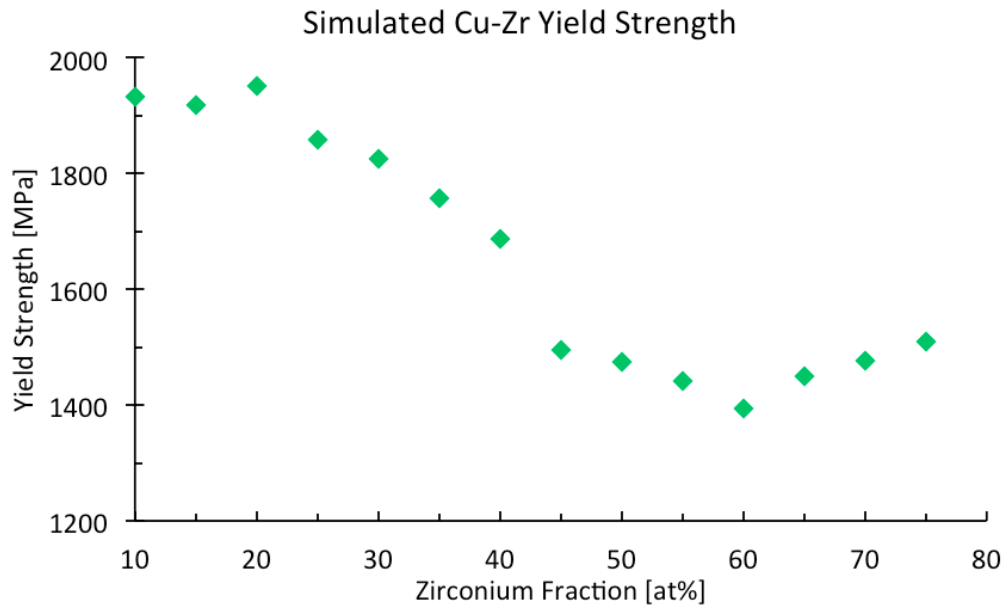

Figure 29: Simulated yield strength of Cu-Zr glasses. The simulated strain rate is 10^{11}/sec. Due to this high strain rate, the yield strengths presented here are overestimates. However, the general compositional trend should be preserved.[71,72]

Cited References

1. Bontha, S., Klingbeil, N. W., Kobryn, P. A. & Fraser, H. L. *J. Mater. Process. Technol.* **178,** 135–142 (2006).
2. Yang, G. L. *et al. Intermetallics* **22,** 110–115 (2012).
3. Zheng, B., Zhou, Y., Smugeresky, J. E. & Lavernia, E. J. *Metall. Mater. Trans. A* **40,** 1235–1245 (2009).
4. Petters, R., Stoica, M., Scudino, S., Pauly, S. & Lo, L. *Mater. Today* **16,** 37–41 (2013).
5. Sun, H. & Flores, K. M. *Metall. Mater. Trans. A* **41,** 1752–1757 (2010).
6. Banerjee, R., Collins, P. C., Bhattacharyya, D., Banerjee, S. & Fraser, H. L. *Acta Mater.* **51,** 3277–3292 (2003).
7. Collins, P. C., Banerjee, R., Banerjee, S. & Fraser, H. L. *Mater. Sci. Eng. A* **352,** 118–128 (2003).
8. Carvalho, P. M. *et al. Surf. Coatings Technol.* **72,** 62–70 (1995).
9. Vilar, R. & Colaco, R. *Surf. Coatings Technol.* **203,** 2878–2885 (2009).
10. Zhang, Y. Z., Meacock, C. & Vilar, R. L *Mater. Des.* **31,** 3891–3895 (2010).
11. Hofmann, D. C. *et al. Sci. Rep.* **4,** 5357 (2014).
12. Banerjee, R., Nag, S. & Fraser, H. L. *Mater. Sci. Eng. C* **25,** 282–289 (2005).
13. Wang, Q. *et al.* Cu-Zr-Al(Ti) *Intermetallics* **15,** 711–715 (2007).
14. Inoue, a, Zhang, W., Zhang, T. & Kurosaka, K. *Acta Mater.* **49,** 2645–2652 (2001).

15. Li, A. Y., Guo, Q., Kalb, J. A., Thompson, C. V & Li, Y. *Science (80-.).* **322,** 1816–1819 (2008).
16. Xu, D., Lohwongwatana, B., Duan, G., Johnson, W. L. & Garland, C. *Acta Mater.* **52,** 2621–2624 (2004).
17. Ausserre, D. & Valignat, M. P. *Nano Lett.* **6,** 1384–1388 (2006).
18. Wang, D. *et al. Appl. Phys. Lett.* **84,** 4029 (2004).
19. Sun, H. & Flores, K. M. *J. Mater. Res.* **23,** 2692–2703 (2011).
20. Chen, B. Q. *et al. J. Alloys Compd.* **511,** 215–220 (2012).
21. Ding, S., Gregoire, J., Vlassak, J. J. & Schroers, J. *J. Appl. Phys.* **111,** 1–7 (2012).
22. Wang, W. H., Lewandowski, J. J. & Greer, a. L. *J. Mater. Res.* **20,** 2307–2313 (2005).
23. Duan, G. *et al. Phys. Rev. B* **71,** 224208 (2005).
24. Johnson, W. L. Science and Technology. **1,** (1999).
25. Hofmann, D. C. *et al. Nature* **451,** 1085–9 (2008).
26. Schuh, C., Hufnagel, T. & Ramamurty, U. *Acta Mater.* **55,** 4067–4109 (2007).
27. Demetriou, M. D. *et al. Nat. Mater.* **10,** 123–8 (2011).
28. Schroers, J. *Adv. Mater.* **22,** 1566–97 (2010).
29. Wang, W. H., Dong, C. & Shek, C. H. *Mater. Sci. Eng. R Reports* **44,** 45–89 (2004).
30. Löffler, J. F. *Intermetallics* **11,** 529–540 (2003).
31. Xu, J. & Ma, E. *J. Mater. Res.* **29,** 1489–1499 (2014).
32. Gludovatz, B. *et al. Proc. Natl. Acad. Sci. U. S. A.* **110,** 18419–24 (2013).
33. Lewandowski *, J. J., Wang, W. H. & Greer, A. L. *Philos. Mag. Lett.* **85,** 77–87 (2005).
34. Greaves, G. N., Greer, A. L., Lakes, R. S. & Rouxel, T. *Nat. Mater.* **10,** 986–986 (2011).
35. Wang, Q. *et al. Sci. Rep.* **4,** 4757 (2014).
36. Wagner, H. *et al. Nat. Mater.* **10,** 439–42 (2011).
37. Ding, J., Patinet, S., Falk, M. L., Cheng, Y. & Ma, E. *Proc. Natl. Acad. Sci.* **111,** 14052–14056 (2014).
38. Oliver, W. C. & Pharr, G. M. *J. Mater. Res.* **7,** 1564–1583 (1992).
39. Deng, Y. P. *et al. Intermetallics* **15,** 1208–1216 (2007).
40. Dmowski, W., Iwashita, T., Chuang, C.-P., Almer, J. & Egami, T. *Phys. Rev. Lett.* **105,** 205502 (2010).
41. Fan, Y., Iwashita, T. & Egami, T. *Phys. Rev. E* **89,** 1–7 (2014).
42. Mizuno, H., Mossa, S. & Barrat, J. L. *Phys. Rev. E* **87,** 1–12 (2013).
43. Mizuno, H., Mossa, S. & Barrat, J.-L. *Europhysics Lett.* **104,** 56001 (2013).
44. Tsamados, M., Tanguy, A., Goldenberg, C. & Barrat, J. L. *Phys. Rev. E* **80,** 1–17 (2009).
45. Daw, M. S., & Baskes, M. I. (1984). Physical Review B, 29(12), 6443.
46. Foiles, S., Baskes, M. I., & Daw, M. (1986). Physical Review B, 33(12), 7983.
47. Daw, M. S., Foiles, S. M., & Baskes, M. I. (1993). Materials Science Reports, 9(7-8), 251–310.
48. Chris H. Rycroft, Voro++: A three-dimensional Voronoi cell library in C++, Chaos 19, 041111 (2009). math.lbl.gov/voro++/
49. Frank, F. C. (1952). Proceedings of the Royal Society A: Mathematical, Physical and Engineering Sciences, 215(1120), 43–46.
50. A. Inoue, A. Katsuya, A. Amiya, T. Masumoto, Mater Trans 1995;36(7):866–75.
51. Miracle, D. B., Sanders, W. S., & Senkov, O. N. (2003). Philosophical Magazine, (2012), 37–41.
52. Cheng, Y. Q., & Ma, E. (2011). 56(4), 379–473.

53. Angell, C. A. (1988). J. Phys. Chem. Solids, 49(8), 863–871.
54. Park, E. S., Na, J. H., & Kim, D. H. (2007). Applied Physics Letters, 91(3), 031907.
55. Senkov, O. N. (2007). Physical Review B, 76(10), 104202.
56. Mauro, N. A. et al. (2014). Nature Communications 5, 4614.
57. Sheng, H. W., Luo, W. K., Alamgir, F. M., Bai, J. M. & Ma, E. (2006) Nature 439, 419.
58. Yu, J. Z., Tsai, A. P., Masumoto, T., & Kawazoe, Y. (1997). Landolt-Bornstein: Phase Diagrams and Physical Properties of Nonequilibrium Alloys. Springer-Verlag.
59. Johnson, R. (1989). Physical Review B, 39(17), 12554.
60. Williams, P. L., Mishin, Y., Hamilton, J. C., Model. Simul. Mater. Sci. 14(5), 817.
61. Guerdane and Teichler. PRB 65, 014203 (2001).
62. Bailey, Schiotz, Jacobsen. PRB 69, 144205 (2004).
63. Russew, K., Stojanova, L., Yankova, S., Fazakas, E., & Varga, L. K. (2009). Thermal behavior and melt fragility number of Cu 100-x Zr x glassy alloys in terms of crystallization and viscous flow. Journal of Physics: Conference Series, 144, 012094.
64. Mattern, N., Schops, A., Kuhn, U., Acker, J., Khvostikova, O., & Eckert, J. (2008). Structural behavior of CuxZr100−x metallic glass (x=35−70). Journal of Non-Crystalline Solids, 354(10-11), 1054–1060.
65. Gargarella, P., Kiminami, C. S., de Oliveira, M. F., Bolfarini, C., & Botta, W. J. (2009). Materials Science and Engineering A, 512(1-2), 53–57.
66. Sheng, H. W., Ma, E., Liu, H. Z., & Wen, J. (2006). Pressure tunes atomic packing in metallic glass. Applied Physics Letters, 88(17), 20–23.
67. Li, Y., Guo, Q., Kalb, J., & Thompson, C. V. (2008). Matching glass-forming ability with the density of the amorphous phase. Science, 322(5909), 1816–9.
68. Y. Calvayrac, J. P. Chevalier, M. Harmelin, A. Quivy, J. Bigot, Philos. Mag. B 48, 323 (1983)
69. Mendelev, Ott, Heggen, Feuerebacher, Kramer et al: J. Appl. Phys. 104, 123532 (2008).
70. Guang-Hai, Hui, Fu-Jiu, Meng-Fen, Yi-Long: Chinese Physics B. Vol. 17, No. 1 (2008).
71. Mendelev, Ott, Heggen, Feuerebacher, Kramer et al: J. Appl. Phys. 104, 123532 (2008).
72. Guang-Hai, Hui, Fu-Jiu, Meng-Fen, Yi-Long: Chinese Physics B. Vol. 17, No. 1 (2008).

At OSU, one graduate student, David Riegner, has been trained by PI Windl to perform all atomistic simulations. In collaboration with former student Logan Ward, a NDSEG Fellow, David has also developed the RAMPAGE potentials.

In collaboration with Dr. Steve Niezgoda at OSU, student Mengfei Yuan has been trained in Abaqus modeling to develop the penetrator model.

At WUSTL, student Peter Tsai has been trained by co-PI Flores to be proficient in LENS deposition. He has also collaborated with student Kelly Kranjc to determine mechanical properties with nanoindentation.

The PIs and their students have participated in a number of conferences during the course of the reporting period:

Atomistic Modeling of Metallic Glass Formation Processes	2/20/15	Hayes Graduate Research Forum (Ohio State)	Columbus, OH	D. Riegner, L. Ward, K. M. Flores, W. Windl
Atomistic Modeling of Metallic Glass Formation Processes	3/16/15	TMS 2015	Orlando, FL	D. Riegner, L. Ward, K. M. Flores, W. Windl
Computationally Efficient Method to Generate Multi-Component EAM Potentials	3/16/15	TMS 2015	Orlando, FL	D. Riegner, L. Ward, W. Windl
A Combinatorial Approach to Designing Metallic Glass Alloys	3/16/15	TMS 2015	Orlando, FL	Peter Tsai, Katharine Flores
Laser Deposition as a Combinatorial Tool for Discovering New Metallic Glass Alloys	3/18/15	TMS 2015	Orlando, FL	Peter Tsai, Katharine Flores
Atomistic Modeling of Metallic Glass Formation Processes	5/13/15	Ohio State Materials Week	Columbus, OH	D. Riegner, L. Ward, K. M. Flores, W. Windl
Atomistic Modeling of Metallic Glass Formation Processes	6/4/15	Ohio Supercomputer Center State User's Group Meeting	Columbus, OH	D. Riegner, L. Ward, K. M. Flores, W. Windl

Atomistic Modeling of Metallic Glass Formation Processes	10/2/15	Graduate Engineering Research Colloquium	Columbus, OH	D. Riegner, L. Ward, K. M. Flo- res, W. Windl

How have the results been disseminated to communities of interest?
If there is nothing significant to report during this reporting period, state "Nothing to Report."
Describe how the results have been disseminated to communities of interest. Include any outreach activities that have been undertaken to reach members of communities who are not usually aware of these research activities, for the purpose of enhancing public understanding and increasing interest in learning and careers in science, technology, and the humanities.

Nothing to report.

What do you plan to do during the next reporting period to accomplish the goals?
If there are no changes to the agency-approved application or plan for this effort, state "No Change."
Describe briefly what you plan to do during the next reporting period to accomplish the goals and objectives.

Project complete.

Appendix – Simulation Details and Constitutive Description of Materials
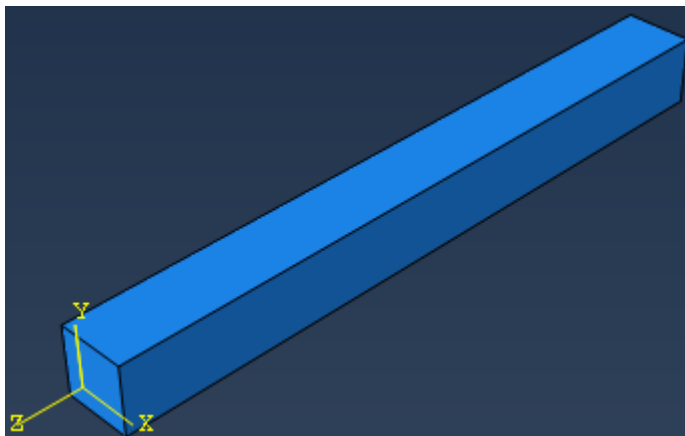
1.1 Units used in Abaqus

Length	Meter
Force	Newton
Time	Second
Mass	Kg
Density	Kg/m^3
Stress	N/m^2
Young's Moduli	N/m^2

1.2 Part and Assembly

1.2.1 Metallic Projectile
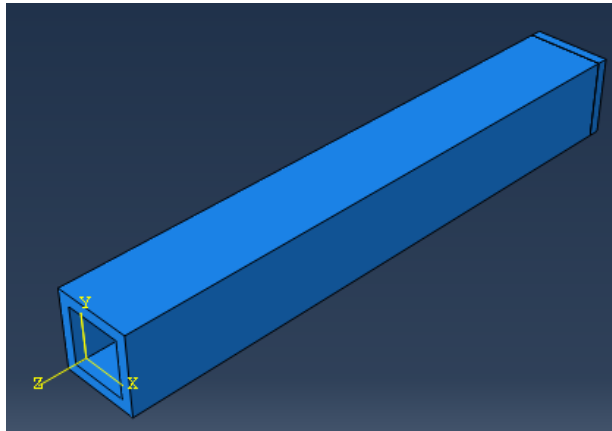
See figure 4

1.2.2 Sand

Material: Sand

(Eulerian Part)

Section: 10×10

Length: 50

The Eulerian part can be divided into several layers with void, full or discrete material.

1.2.3 Concrete Bunker

Material: Concrete (Lagrangian Part)

In order to make the sand part are endless, there is a concrete confinement outside the lateral side of sand part.

Outer section: 12×12

Inner section: 10×10

Length: 51

Thickness: 1

1.3 Material Properties

1.3.1 Concrete

1.3.1.1 Elastic, Thermal and Electrical Properties

The material properties used for concrete bunker are come from examples in ABAQUS example manual. Properties of concrete are same as Koyna dam, which is a classic example used for seismic analysis.

Density	2643
Elastic Moduli	31.02E+09
Poisson ratio	0.2
Conductivity	0.7
Specific Heat	880

1.3.1.2 Concrete Damage Plasticity

(1) Plasticity

Dilation Angle	Eccentricity	f_{b0}/f_{c0}	K	Viscosity parameter
36.31	0.1	1.15	0.0007	0(default)

(2) Compressive Behavior

Yield Stress	Inelastic Strain
1.30E+07	0
2.41E+07	0.001

(3) Tensile behavior (Type: Displacement)

Yield stress	Displacement	Damage Parameter
2.90E+06	0	0
1.94E+06	6.62E-05	0.381217
1.30E+06	0.00012286	0.617107
8.73E+05	0.000173427	0.763072
5.86E+05	0.00022019	0.853393
3.92E+05	0.000264718	0.909282
2.63E+05	0.000308088	0.943865
1.76E+05	0.00035105	0.965265
1.18E+05	0.000394138	0.978506
7.92E+04	0.000437744	0.9867
5.31E+04	0.000482165	0.99177

1.3.2 Sand

1.3.2.1 Elastic, Thermal and Electrical Properties

Most of the general properties of sand are estimated from the average value of dry sand.

Density	5000
Shear Moduli	5.0E+07
Conductivity	0.2
Specific Heat	830

1.3.2.2 Equation of State

The equation of state, compaction state, are especially coming from Brown, J. L. et al. (2007). Linear u_s-u_p relationship is used for sand, and the Gruneisen parameter, Γ_0, is assumed to be 1.0 in this model.

u_s-u_p Liner Relationship		
$$u_s = c_0 + s\,u_p = 0.243 + 2.348u_p$$		
Reference speed (c_0, m/s)	Slope (s)	Gruneisen parameter (Γ_0)
243	2.348	1.0
$P-\alpha$ EOS Compaction		
Reference sound speed in the porous material , c_e, m/s		145.8

Value of the porosity of the unloaded material, n_0	0.4
Pressure required to initialized plastic behavior, p_e, Pa	0.9E+06
Compaction pressure at which all pores are crushed , p_s, Pa	1.13E+09

1.3.3 Metallic Glass ($Zr_{55}Al_{10}Ni_5Cu_{30}$)

Most of the material properties of metallic glass, $Zr_{55}Al_{10}Ni_5Cu_{30}$, are determined by Mashimo, T. et al. (2006). Some undetermined parameters are instead of common glass properties because of the absence of experiments. The plasticity, failure model, and the equation of state are also assumed from experimental data.

1.3.3.1 Mechanical Properties

1.3.3.2 Elastic, Thermal and Electrical Properties

Density	6790
Elastic Moduli	85.7E+09
Poisson ratio	0.37
Shear Moduli	31.28E+09
Conductivity	5.00
Specific Heat	700

1.3.3.3 Johnson – Cook Plasticity

Johnson-Cook Plasticity is suitable for high-strain rate deformation of most metals, and most applicable to dynamic failures. Johnson- Cook plasticity model belongs to Mises plasticity model, and must be in conjunction with either the linear elastic material model or equation of state. In this simulation, the Mie-Gruneisen equation of state material model is selected to establish the hydrodynamic material model.

The stress of metallic glass can be assumed to be the following equation.

$$\sigma = [A + B\,(\bar{\varepsilon}^{pl})^n][1 + C\ln{(\dot{\varepsilon})}][1 + \hat{T}^m]$$

where $\bar{\varepsilon}^{pl}$ is the equivalent plastic strain and A, B, n and m are material parameters measured at or below the transition temperature. C, is the material parameter depend on strain rate, and $\dot{\varepsilon}$ is strain rate. The temperature dependence term is defined as the following equation.

$$\hat{T} = \begin{cases} 0 & for\ T < T_{tr} \\ (T - T_{tr})/(T_m - T_{tr}), & for\ T_{tr} < T < T_m \\ 1 & for\ T > T_{tr} \end{cases}$$

where $\hat{T}$ is the non-dimensional temperature, T is the current temperature, T_m is the melting temperature, and T_{tr} is the transition temperature.
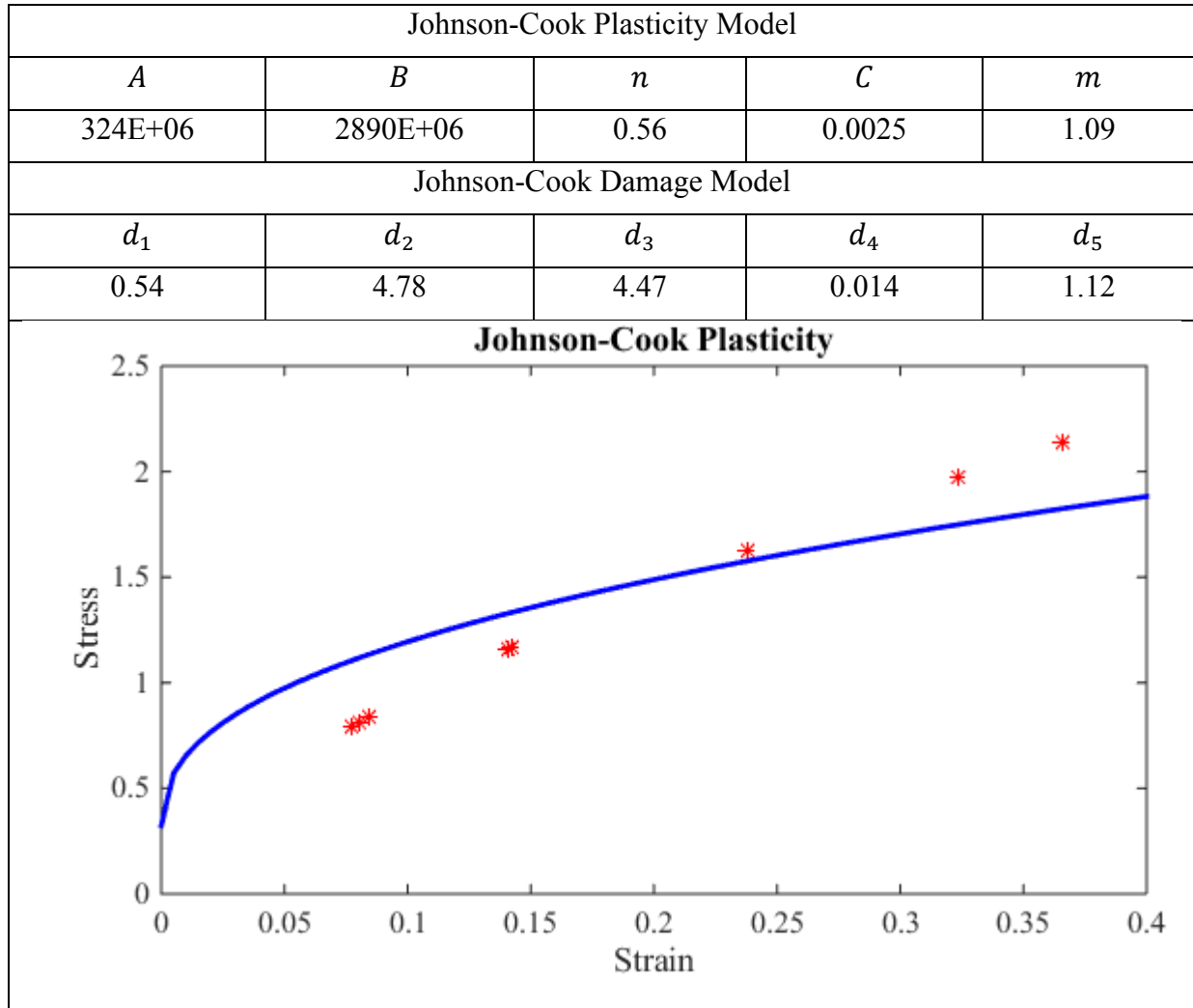
In Abaqus explicit, Johnson-Cook plasticity can be conjunction with the progressive damage and failure model, which based on equivalent plastic strain. Johnson-Cook damage model can also
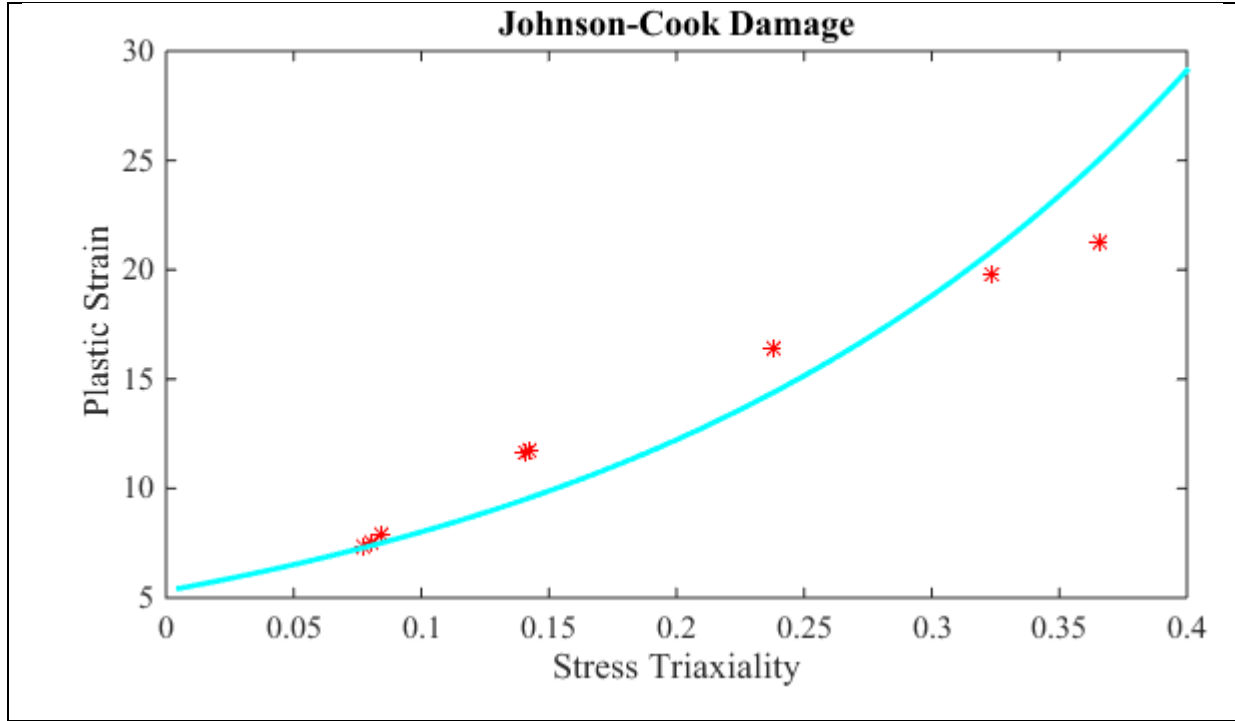
depend strain rate and temperature as well. The dependencies are assumed to be the forma of the following equation.

$$\bar{\varepsilon}_f^{pl} = [d_1 + d_2 Exp(d_3\mu)][1 + d_4 ln\dot{\varepsilon}][1 + d_5\hat{T}]$$

Where, d_1, d_2, d_3, d_4, and d_5 are failure parameters. In Abaqus simulation, the elements that meet the failure criterion are deleted.

The material parameter used in this simulation is displayed in the following table.

Johnson-Cook Plasticity Model				
A	B	n	C	m
324E+06	2890E+06	0.56	0.0025	1.09
Johnson-Cook Damage Model				
d_1	d_2	d_3	d_4	d_5
0.54	4.78	4.47	0.014	1.12

Johnson-Cook Damage — Plastic Strain vs Stress Triaxiality

1.3.3.4 Gruneisen Equation of State

The tabular function values, f_1 and f_2, are calculated from results from Hugoniot compressive test in Mashimo, T. et al. (2006).

$$P(\varepsilon_{vol}) = f_1(\varepsilon_{vol}) + f_2\, E_m$$

The data of Hugoniot compressive test are shown in table below. The Gruneisen parameter, Γ_0, is assumed to be 1.5 which is identical to common glass temperately.

Hugoniot compressive test							
No.	Specimen thickness (m)	Initial density (m/s)	Impact velocity (m/s)	Shock velocity (m/s)	Particle Velocity (m/s)	Pressure (GPa)	Density (Kg/m³)
1	1.816E-03	6790	670	5260	171	6.11	7020
2	2.082 E-03	6750	758	5300	185	6.62	6990
3	1.810 E-03	6760	1033	5360	160	5.8	6970
4	1.819 E-03	6750	1169	5290	380	13.57	7270
5	1.825 E-03	6740	1193	5230	390	13.75	7280
6	1.831 E-03	6760	1081	5139	767	26.65	7950
7	1.826 E-03	6750	1547	5255	1103	39.12	8540
8	1.828 E-03	6740	1756	5400	1248	45.42	8770

1.3.3.5 Drucker – Prager Plasticity

Shear criterion: exponent form (developed from Mohr-coulomb yield surface)

(1) Dilation angle

Dilation angle, ψ, measured in the p–q plane at high confining pressure, unit in degree.

The angle of dilation controls an amount of plastic volumetric strain developed during plastic shearing and is assumed constant during plastic yielding. The value of $\psi = 0$ corresponds to the volume preserving deformation while in shear.

(2) Flow potential eccentricity

Flow potential eccentricity, ϵ, defines the eccentricity between yielding function and its asymptote.

(3) Yield surface

The Drucker-Prager plasticity is established on yield surface.

$$q = \sigma_1 - \sigma_3$$

$$p = -\frac{1}{3}(2\sigma_1 + \sigma_3)$$

$$p_t = a\sigma_c^b + \frac{1}{3}\sigma_c \, (depends \; on \; hardening)$$
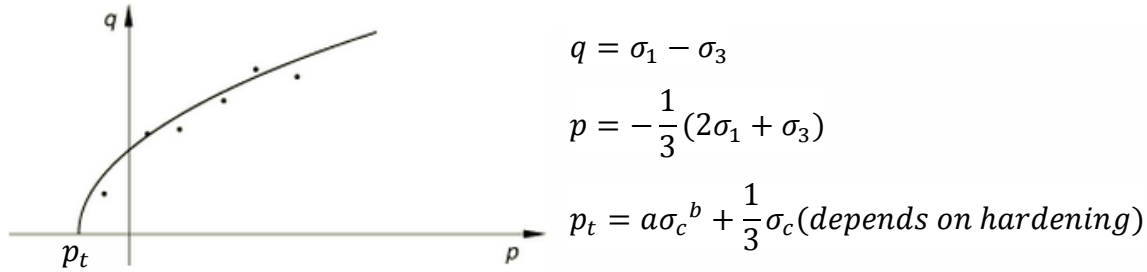
According to the confining stress, σ_1, and loading stress, σ_3, $\sigma_1 = \sigma_2 \neq \sigma_3$, the yield surface of material can be established by finding a best fit curve. Equation 2.1 is the exponential function of yield surface for a material.

$$F = aq^b - p - p_t = 0 \qquad\qquad (0.1)$$

The material parameters a, and b can be given directly, or subscribed from triaxial test alternatively, $a = \frac{P_{HEL}}{(\sigma_{HEL}A)^{1/N}}$, $b = \frac{1}{N}$. In this simulation, the value of a and b are estimated from the Mohr Coulomb yield surface of $Zr_{55}Al_{10}Ni_5Cu_{30}$.

1.3.3.6 Damage: Ductile Damage for Metal

The triaxial test (or compressive and tensile tests), the flyer plate test, and ballistic penetration test are required to build the JH-2 damage model for a material. The Hugoniot state, pressure, and some common material properties of metallic Glass ($Zr_{55}Al_{10}Ni_5Cu_{30}$) can be determined by Mashimo T. et al. (2006). Holmquist, T.J. et al. (1995) described the method and results of establishing the JH-2 model of float glass. Combine with Drucker-Prager Model and Mie Gruneisen EOS, the JH-2 model can calibrate in ductile damage model in Abaqus. JH-2 model is suitable for brittle material, progressive damage, large pressure and high strain rate. All the parameters used in JH-2 model can be determined from Mashimo T. et al. (2006) and Lund, A. C. and Schuh, C. A. (2003). Equations 2.2 and 2.3 show the mathematical relationship between constant pressure, P, fracture strain, $\bar{\varepsilon}^{pl}$, stress triaxiality, η, and strain rate, $\dot{\bar{\varepsilon}}$. The continuous relationship between fracture strain, stress triaxiality, and strain rate can be determined according

to the Hugoniot test from Mashimo T. et al. (2006), which offers eight results of flyer plate tests with similar strain rate, which can determine a continuous relationship between stress triaxiality, strain rate, and fracture strain.

$$\bar{\varepsilon}^{pl}(i) = D_1 \left(\frac{P(i)}{P_{HEL}} + \frac{T}{P_{HEL}} \right)^{D_2}$$ (0.2)

$$\eta(i) = -\frac{P(i)}{\sigma_{intact}} = -\frac{P(i)}{\sigma_{HEL} \left[A \left(\frac{P(i)}{P_{HEL}} + \frac{T}{P_{HEL}} \right)^{N} \right] \left[1 + Cln\left(\dot{\bar{\varepsilon}}(i) \right) \right]}$$ (0.3)
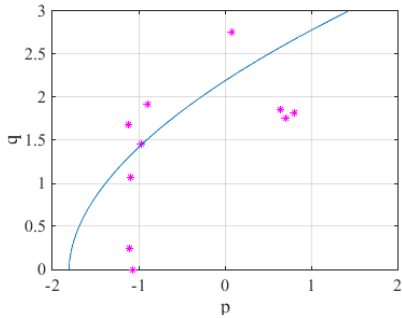
where, P_{HEL} is pressure at Hugoniot elastic limit; σ_{HEL} is stress at Hugoniot elastic limit; $T = p_t$

Three viable are required in ABAQUS shown below.

Fracture Strain $(\bar{\varepsilon}^{pl})$	Stress Triaxiality (η)	strain rate $(\dot{\bar{\varepsilon}}^{pl})$	Round off $(\dot{\bar{\varepsilon}}^{pl})$
0.36579	-21.2643	88398	1.00E+05
0.32387	-19.7921	88857	1.00E+05
0.23781	-16.4196	94163	1.00E+05
0.14233	-11.7558	208906	2.00E+05
0.14093	-11.6758	213699	2.00E+05
0.08453	-7.89775	418897	5.00E+05
0.08016	-7.53763	604053	5.00E+05
0.07748	-7.31234	682713	5.00E+05

Note: strain rate inputted in ABAQUS are all assumed to be identical for enough information.

| Metallic Glass ($Zr_{55}Al_{10}Ni_5Cu_{30}$)	
Density, ρ_0	6750Kg/m^3
Young's Moduli, E	85.7GPa
Poisson Ratio, v	0.37
Shear Moduli, G	31.28GPa
Strength Model	
A	0.6027
N	0.5393
C (consider with different stain rate)	-
Normalized intact strength: $\sigma_i^* = A(P^* + T^*)^N (1 + C \ln \dot{\varepsilon})$	

Tensile strength, σ_t	1.53Gpa
Compressive strength, σ_c	1.77Gpa
HEL	11.07 GPa
Pressure at HEL, P_{HEL} $P = K_1\mu + K_2\mu^2 + K_3\mu^3$	4.87 GPa
Stress at HEL, σ_{HEL}	6.2GPa
Volume strain at HEL, μ_{HEL} $\mu = \dfrac{\rho}{\rho_0} - 1$	0.0392

Drucker-Prager Plasticity

Yield Surface: $F = aq^b - p - p_t = 0,$ $p = -\dfrac{1}{3}(2\sigma_1 + \sigma_3),$ $q = (\sigma_1 - \sigma_3)$	
$a = \dfrac{P_{HEL}}{(\sigma_{HEL}A)^{1/N}}$	0.4223
$b = \dfrac{1}{N}$	1.8452
$p_t = a\sigma_c{}^b + \dfrac{1}{3}\sigma_c$	1.8073 Gpa
Dilation angle, ψ	0(default)
Flow eccentricity , ϵ	0.1(default)

Equation of State : $P(\varepsilon_{vol}) = f_1(\varepsilon_{vol}) + f_2\, E_m$

K_1 (Bulk Moduli)	110.8 GPa
K_2	480.6 GPa
K_3	-1201 GPa

Pressure, P (GPa)

Material Constants

$K_1 = 110.8 GPa$

$K_2 = 480.6 GPa$

$$\mu = \frac{\rho}{\rho_0} - 1$$
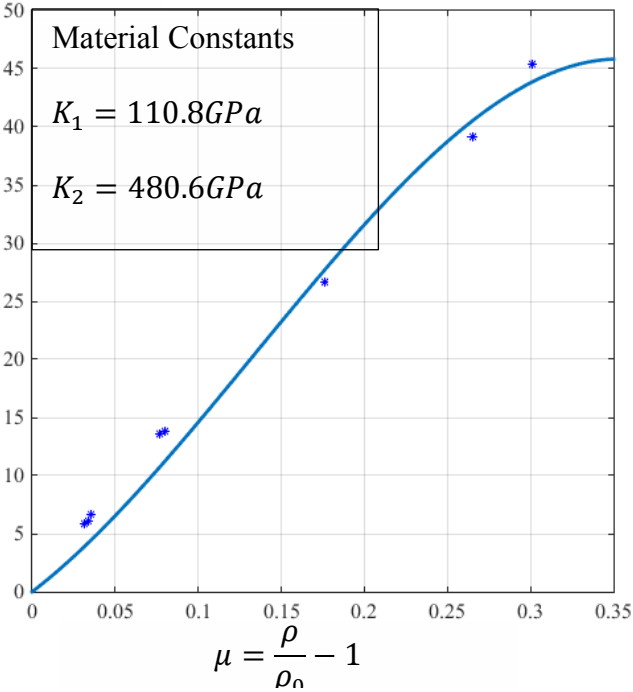
Damage Model (use model of glass)

D_1 (glass)	0.043
D_2 (glass)	0.85

σ

$\bar{\sigma}$

(D=0)

σ_{y0}

$D\bar{\sigma}$

σ_0

E   E   (1-D)E

$\bar{\varepsilon}_0^{pl}$ $\bar{\varepsilon}_f^{pl}$ ε
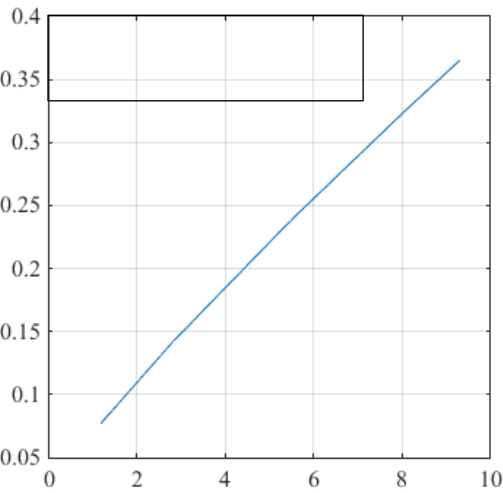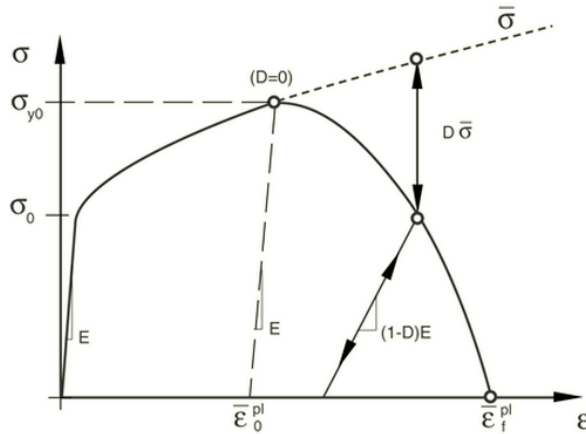
σ_{y0}: yield stress

$\bar{\varepsilon}_0^{pl}$: Equivalent plastic strain at onset of damage

$\bar{\varepsilon}_f^{pl}$: Equivalent plastic strain at failure

The damage evolution parameter, D, can determine how fast it damage.

$$\sigma^* = \sigma_i^* - D\left(\sigma_i^* - \sigma_f^*\right),$$

$D_{max} = 0.5,\ assume\ for\ brittle\ damage$, complete damage at $D = D_{max}$

Hardening:

For compressive criterion, $p_t = a\sigma_c^b + \frac{1}{3}\sigma_c$;

(Yield stress, σ_c is determined by tests, and the corresponding plastic strain is set start from zero.)

Softening:

1.4 Mesh (Explicit)

(1) Element type used for metallic projectile is C3D6. (Lagrangian solid part)

Distortion control=0.1; Element deletion=yes; Max Degradation=0.5 (max is 1);

Seed size=0.025 Element shape=Wedge;

(2) Element type used for concrete bunker is C3D8. (Lagrangian solid part)

Distortion control=0.1; Element deletion=yes; Max Degradation=1;
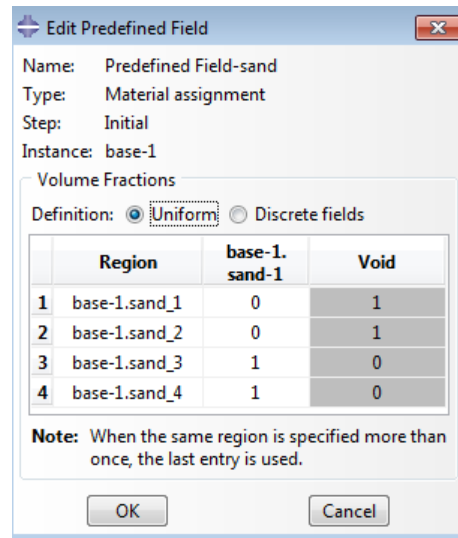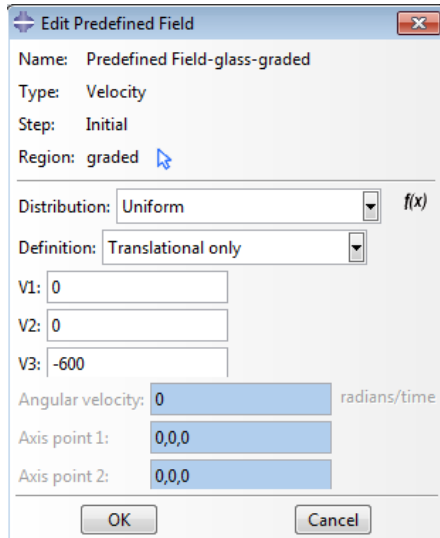
Seed size=0.25; Element shape=Hex;
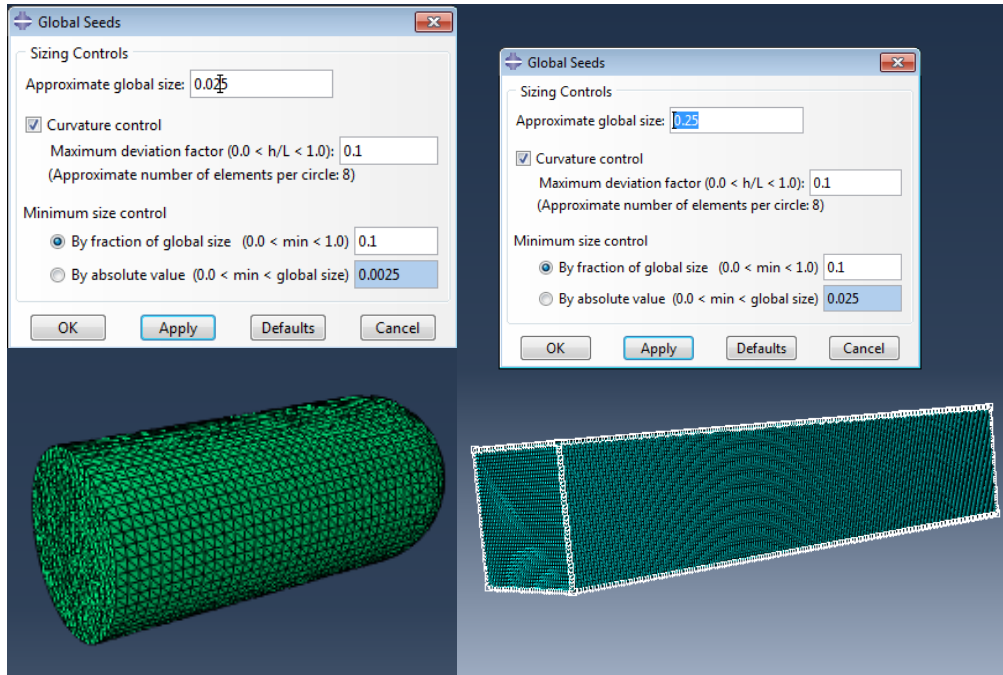
(3) Element type used for sand is C3D6 (Hex). (Eulerian part)
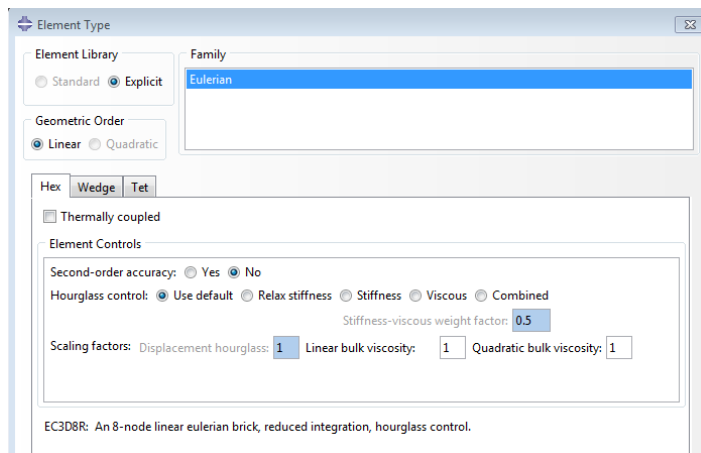
## 1.5 Predefined Fields and Boundary Condition

1.5.1 Initial Condition

The projectile has an initial velocity of 600m/s in z-direction. The Eulerian part is consisted of void parts and sand parts.
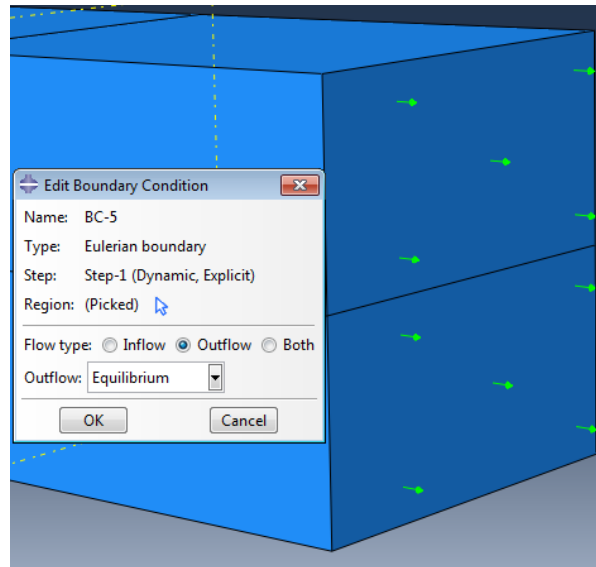

Initial velocity of projectile   Predefined field of Eulerian part

1.5.2 Boundary Condition

The surrounding of concrete model is confined in three directions translation and rotation.

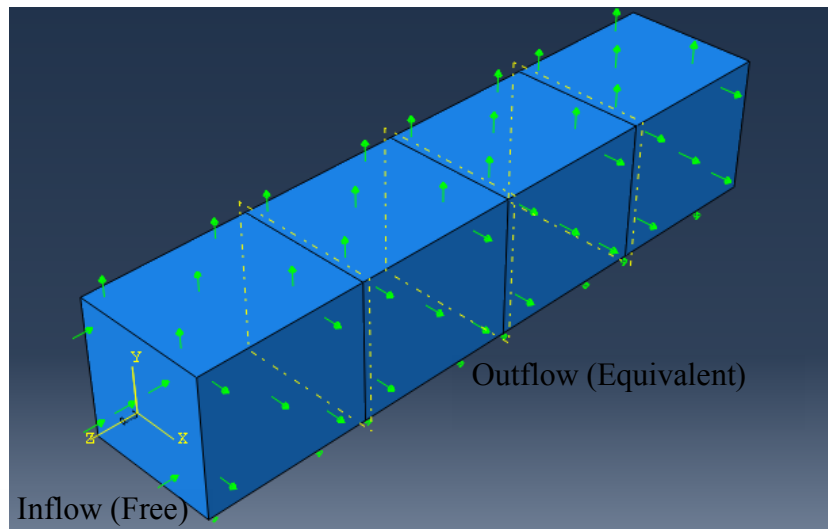The inflow surface and outflow surface of Eulerian part are applied with Eulerian Boundary.
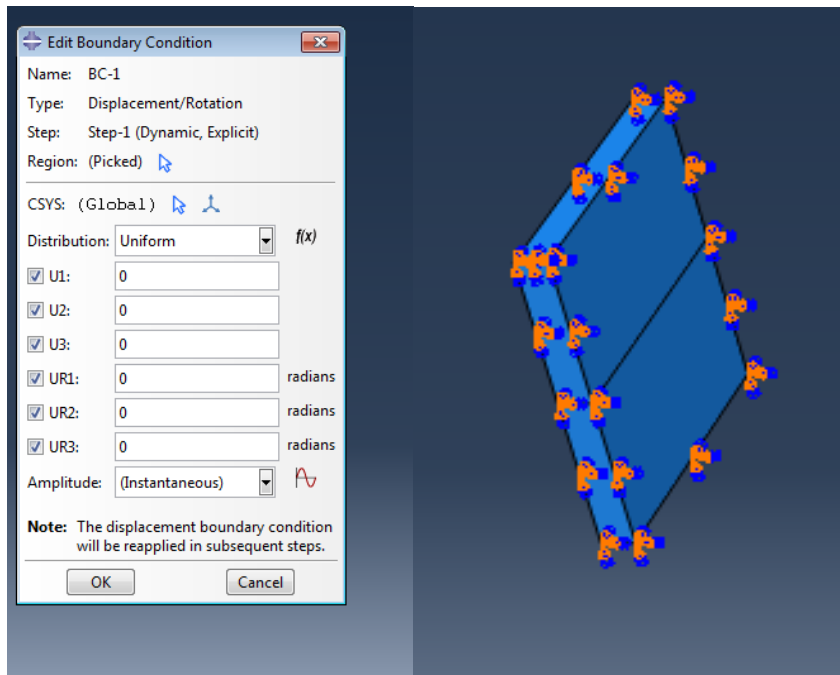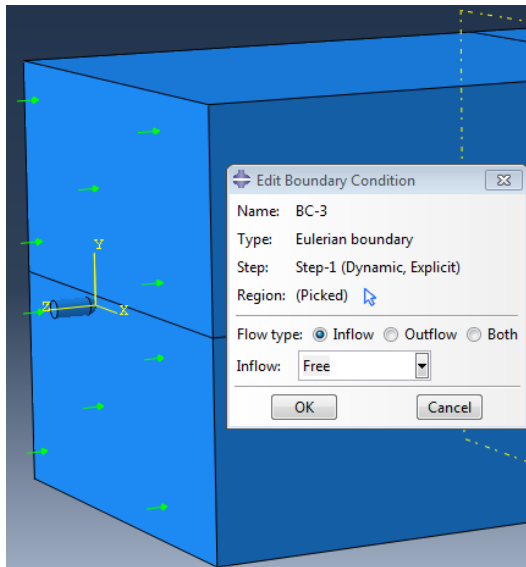
Inflow Surface   Outflow Surface


Outflow (Equivalent)

Inflow (Free)

1.6 Additional Results

1.6.1 Radially Graded Properties

The following figures show effects of bullet with graded properties along thickness. The remark "1" in the figure denotes to larger properties, and "3" denotes to smaller properties. The depth of each situation is listed in the following table.

Original	Density -	Density+	Stiffness-	Stiffness+	Strength-	Strength+
36.5196	35.9109	36.9396	36.5799	36.8868	36.8891	37.8805
-	-1.64%	+1.15%	+0.17%	+1.00%	+1.01%	+3.73%

Graded Properties along thickness(Stiffness)

Graded Properties along thickness
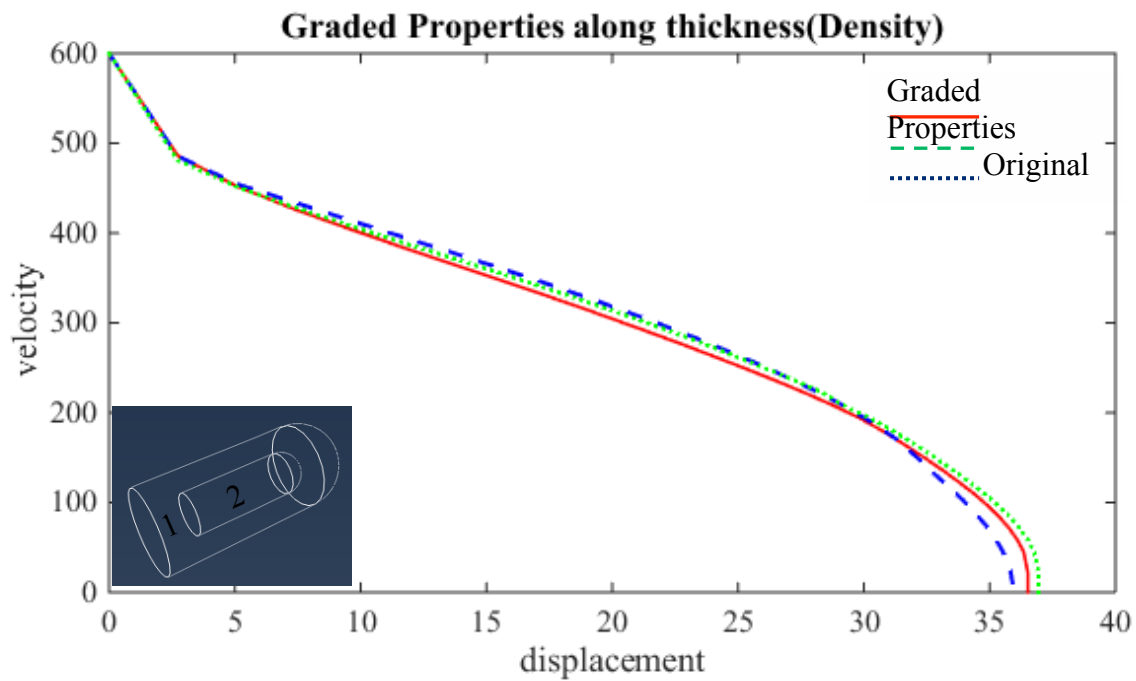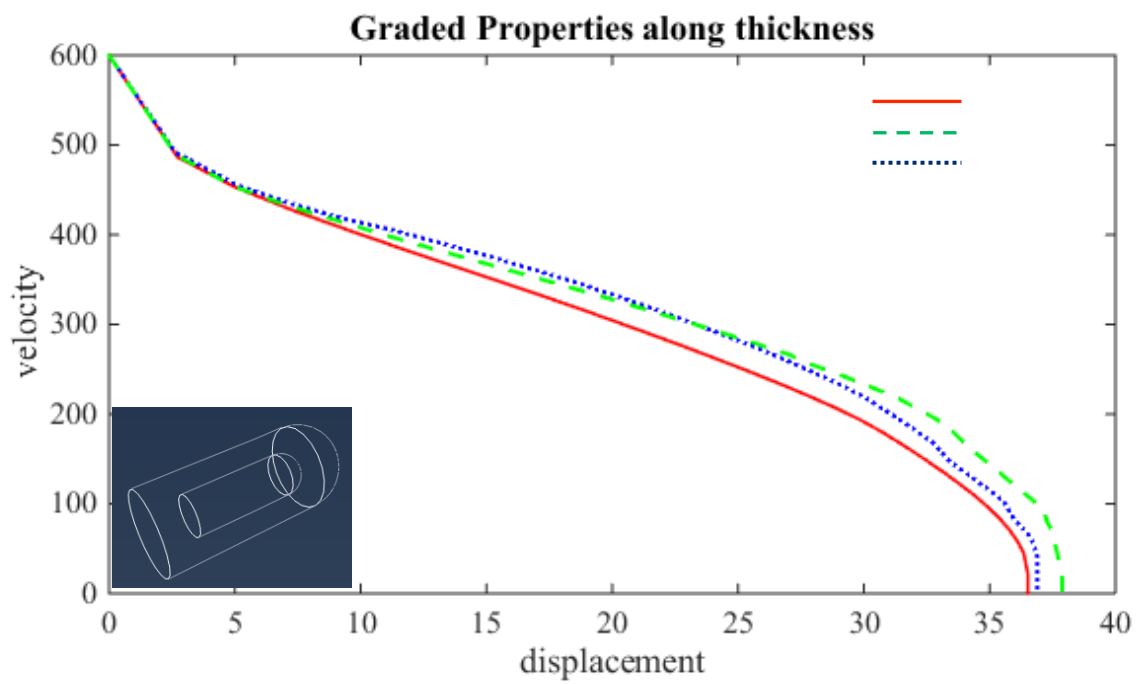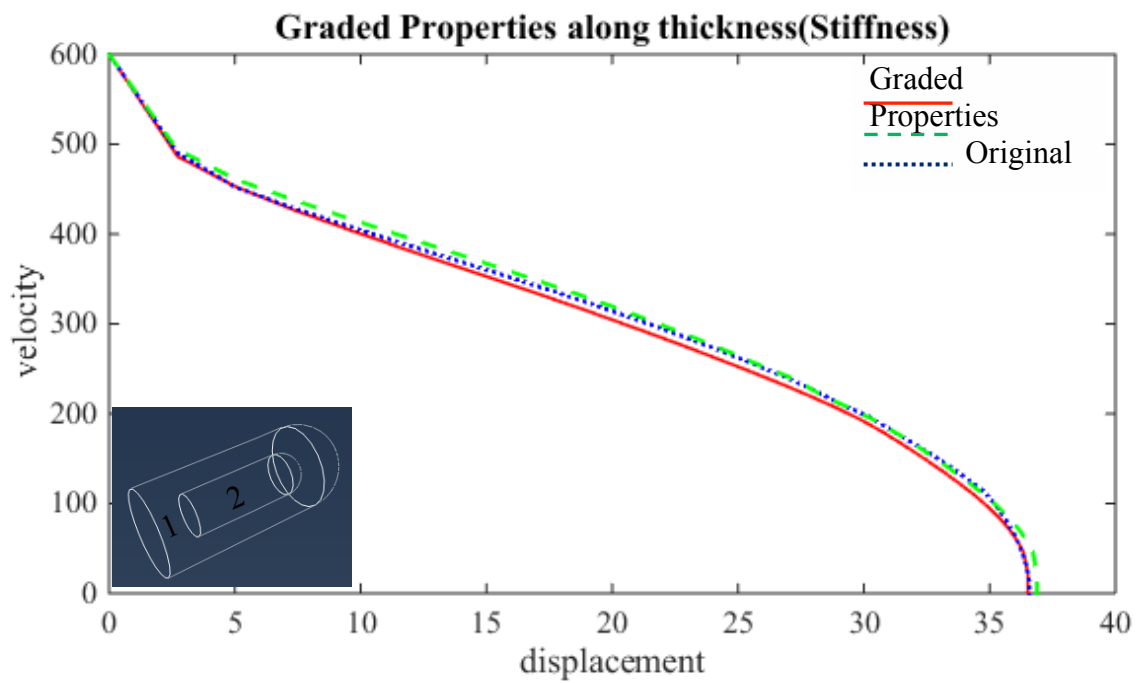
1.6.2   Concrete Penetration

Simulations were performed with concrete slabs at a depths of 20, 25, 30 and 40m. The homogenous projectile was able to penetrate the 20 and 25m deep slabs but not the 30m deep slab. The projectile stopped in the sand before reaching the 40m deep projectile.
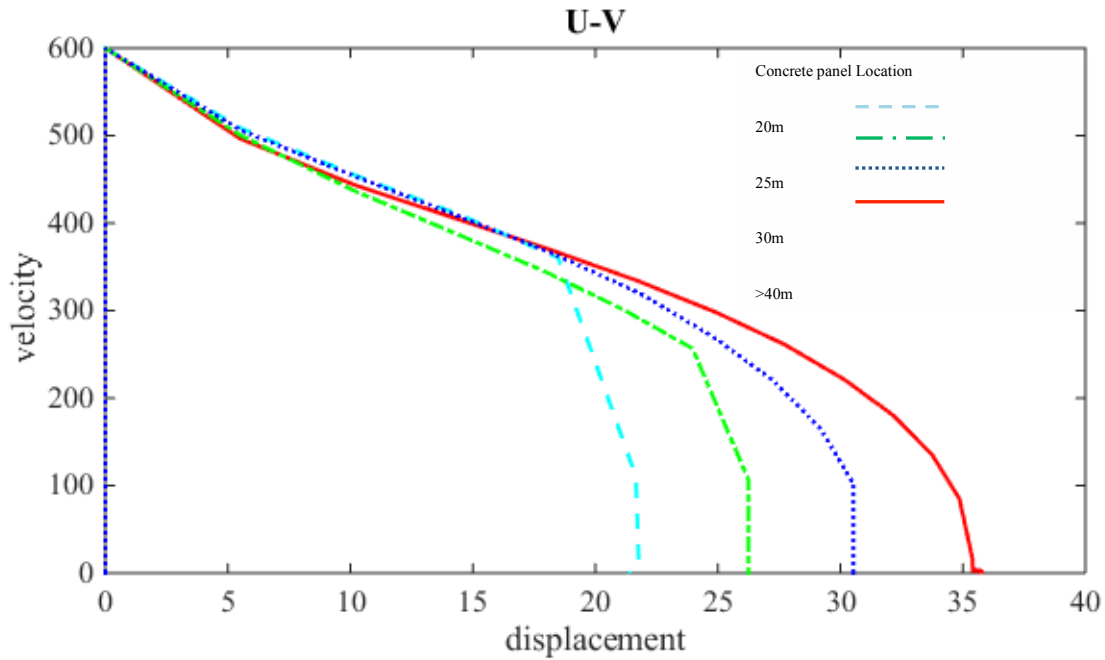
References

Abaqus 6.14 Online Documentation. (2014)

Brown, J. L., Vogler, T. J., Chhabildas, L. C., Reinhart, W. D., Thornhill, T. F. (2007). "Shock Responses of Dry Sand". *SAND2007-3524*. Sandia National Laboratories, Albuquerque, NM.

Chen, Y., Jiang, M. Q., Wei, Y. J., Dai, L. H. (2011). "Failure criterion for metallic glasses". *Philosophical Magazine*, 91(36), 4536-4554.

Cronin, D. S., Bui, K., Kaufmann, C., McIntosh, G., Berstad, T., & Cronin, D. (2003). "Implementation and validation of the Johnson–Holmquist ceramic material model in LS-DYNA". In *4th European LS-dyna users conference*, May, 2003, Vol. 500, 47-60.

Holmquist, T J., Johnson, G. R., Lopatin, C. M., Grady, D. E., and Hertel, E. S. J. (1995). "High Strain Rate Properties and Constitutive Modeling of Glass". In *15th International Symposium on Ballistic*, May, 21-24, 1995, Jerusalem, Israel.

Johnson, G. R. and Holmquist, T. J. (1994). "An Improved Computational Constitutive Model for Brittle Materials," *High Pressure Science and Technology*, 981–984.

Kanomata, T., Sato, Y., Sugawara, Y., Kimura, H. M., Kaneko, T., Inoue, A. (2008). "Specific heat of Zr-based metallic glasses". *Journal of Alloys and Compounds*, 461(1), 39-41.

Louzguine-Luzgin, D. V., Saito, T., Saida, J., Inoue, A. (2008). "Thermal conductivity of metallic glassy alloys and its relationship to the glass forming ability and the observed cooling rates". *Journal of Materials Research*, 23(08), 2283-2287.

Lund, A. C., Schuh, C. A. (2003). "Yield surface of a simulated metallic glass". *Acta materialia*, *51*(18), 5399-5411.

Mashimo, T., Togo, H., Zhang, Y., Uemura, Y., Kinoshita, T., Kodama, M., and Kawamura, Y. (2006). "Hugoniot-compression curve of Zr-based bulk metallic glass". *Applied physics letters*, 89(24), 241904-241904.

Pandey, A. K., Pandey, B. K. (2011). "Theoretical prediction of Gruneisen parameter for bulk metallic glasses". *Journal of Alloys and Compounds*, 509(11), 4191-4197.

DEPARTMENT OF DEFENSE

DEFENSE THREAT REDUCTION
AGENCY
8725 JOHN J. KINGMAN ROAD
STOP 6201
FORT BELVOIR, VA 22060
     ATTN: A. DALTON

DEFENSE TECHNICAL
INFORMATION CENTER
8725 JOHN J. KINGMAN ROAD,
SUITE 0944
FT. BELVOIR, VA 22060-6201
     ATTN: DTIC/OCA

**DEPARTMENT OF DEFENSE
CONTRACTORS**

QUANTERION SOLUTIONS, INC.
1680 TEXAS STREET, SE
KIRTLAND AFB, NM 87117-5669
     ATTN: DTRIAC